Structure and Deformation History of the Rapidly Growing Tainan Anticline at the Deformation Front of the Taiwan Mountain Belt

Maryline Le Béon, Odin Marc, John Suppe, Mong-Han Huang, Shiuh-Tsann Huang, Wen-Shan Chen

HAL Id: insu-03707752
https://insu.hal.science/insu-03707752

Submitted on 29 Jun 2022

Structure and Deformation History of the Rapidly Growing Tainan Anticline at the Deformation Front of the Taiwan Mountain Belt

Maryline Le Béon[1,2] , Odin Marc[3,4,5] , John Suppe[6,7] , Mong-Han Huang[8] , Shiuh-Tsann Huang[9], and Wen-Shan Chen[6]

[1]Department of Earth Sciences, National Central University, Jhongli, Taiwan, [2]Now at Graduate Institute of Applied Geology, National Central University, Jhongli, Taiwan, [3]Helmholtz Centre Potsdam, German Research Center for Geosciences (GFZ), Potsdam, Germany, [4]Now at Department of Earth Sciences, ETH Zurich, Zurich, Switzerland, [5]École et Observatoire des Sciences de la Terre – Institut de Physique du Globe de Strasbourg, Centre National de la Recherche Scientifique UMR 7516, Université de Strasbourg, Strasbourg, France, [6]Department of Earth and Atmospheric Sciences, University of Houston, Houston, TX, USA, [7]Department of Geosciences, National Taiwan University, Taipei, Taiwan, [8]Department of Geology, University of Maryland, College Park, MD, USA, [9]CPC Corporation, Miaoli, Taiwan

Abstract This study aims at further documenting the mechanisms of shortening at the front of fold-and-thrust belts. We focus on an actively growing anticline located at the deformation front of the Taiwan fold-and-thrust belt. Based on a multidisciplinary approach combining mainly subsurface data and geodetic techniques, we show that the Tainan anticline is a pure-shear fault-bend fold growing above a 38–45° west dipping back thrust, the Houchiali fault, rooted on a 3.8-km-deep detachment. The cumulative shortening is estimated at 2–3 km since 310 ± 50 ka, including ~30–50% of horizontal compaction shortening. The significance of the fold is little in terms of total shortening at the scale of the mountain piedmont, yet the Holocene shortening rate of 10.3 ± 1.0 mm/a accounts for 25% of the present-day shortening rate across the piedmont. Earthquake scaling relationships applied to the Houchiali fault predict Mw~6 earthquakes that would occur a lot more frequently than indicated from historical earthquake catalogs. Hence, the aseismic slip behavior observed from geodetic measurements since two decades is a representative behavior of the fault at least at the scale of a few centuries. Our results bear out the dominance of pure-shear folding at the front of fold-and-thrust belts and support horizontal compaction as a significant shortening mechanism. In contrast, the back thrust wedge structure and the aseismic slip are peculiar characteristics that likely arise from the combination of low friction and high-pore pressure related to the thick mudstone formation hosting the wedge and of high syntectonic sedimentation rates.

Plain Language Summary The toe of active mountain belts often concentrates human population, fertile land, and economic centers. They are also the location of active faults that expose the population to seismic hazard. This study investigates how compressive tectonic forces are consumed at the front of mountain belts. We focus on an actively growing anticline located at the front of the Taiwan mountain belt. Based on a multidisciplinary approach combining mainly subsurface data and geodetic techniques, we show that the fold grows by thickening of the geological strata due to the westward displacement of a wedge structure defined by a west dipping fault and a 3.8-km-deep detachment (i.e., a subhorizontal bedding-plane fault). The fold has little significance when considering the history of deformation at the scale of the mountain belt; however, it has been a major player since 10,000 years, as it concentrates 25% of the tectonic activity across the piedmont. The lack of destructive earthquakes in historical accounts during the last 300 years shows that the tectonic forces are mainly consumed by slow and nearly steady free slip on the fault, as observed from geodetic methods during the last two decades, rather than by earthquakes.

1. Introduction

Field observations and geophysical subsurface imaging lead to identifying different styles of fault-related folding to accommodate shortening in various tectonic settings and depositional environments (e.g., Shaw et al., 2005; McClay, 2011). From subaerial fold-and-thrust belts to deep marine accretionary wedges and gravity-driven fold-and-thrust belts, pure-shear detachment folds and pure-shear fault-bend folds are found to be a dominant feature at the deformation front: for example, offshore northwest Borneo (Ingram et al.,

2004), in Cascadia and Nankai accretionary wedges (Gonzalez-Mieres and Suppe, 2006; Suppe et al., 2004), Niger Delta (Corredor et al., 2005), Makran accretionary wedge (Grando and McClay, 2007), southern Tianshan piedmont (Hubert-Ferrari et al., 2007), and Taiwan piedmont (Yue et al., 2011). Pure-shear folds grow by layer-parallel thickening (in many cases of a weak basal layer, the base of which corresponds to a detachment level), leading to progressive limb rotation of the above geological strata and fold widening by kink-band migration (Epard and Groshong, 1993, 1995; Hardy and Connors, 2006; Suppe et al., 2004; Suppe, 2011). As shortening accumulates, the fold limbs steepen, and the fold may evolve into a classical fault-bend fold with a ramp that allows accommodating kilometers of slip (Gonzalez-Mieres and Suppe, 2006; Yue et al., 2011).

This study focuses on the active structures at the deformation front of the southern Taiwan fold-and-thrust belt, in Tainan City. The Taiwan mountain belt results from the collision between the Luzon volcanic arc on the Philippine Sea plate and the South China passive continental margin on the Eurasia plate (Figure 1a). Collision started 5–7 Ma ago (Ho, 1986; Lee et al., 2015; Lin et al., 2003; Suppe, 1984; Teng, 1990) and occurs at a rate of ~89 mm/a based on long-term relative plate motions (Argus et al., 2011). Geodetic surveys at the island scale (Hsu et al., 2009; Lin et al., 2010; Tsai et al., 2015; Yu et al., 1997) show that shortening is mostly consumed along the Longitudinal Valley in eastern Taiwan, considered as the plate suture, and across the Western Foothills that consist in the deformation front.

In southern Taiwan, the edge of the Chinese continental shelf is not involved yet in the collision. Oligocene and Miocene passive-margin normal faults were identified from seismic reflection profiles offshore Tainan and within the Coastal Plain (Liao et al., 2016; Lin, 2001; Lin et al., 2003, 2008; Yang et al., 2006). They trend ~N60°E offshore, along the shelf edge and within the Tainan Basin down the continental slope, and ~N75°E within the Coastal Plain north of Tainan (Figure 1a). Therefore, they are oblique to nearly parallel to the direction of convergence and at the origin of a southward deepening of the basin, with some irregularities that probably affected the development of the foreland basin and of the fold-and-thrust belt during the Pliocene and the Quaternary (Biete et al., 2018; Brown et al., 2017; Lin et al., 2003; Yang et al., 2016).

In southwestern Taiwan, at the latitude of Tainan City, ~40 mm/a shortening is consumed across the Western Foothills, from the coastline to ~40 km east, based on Global Positioning System (GPS) measurements (e.g., Hsu et al., 2009; Lin et al., 2010; Tsai et al., 2015; Figure 1). Downtown Tainan is located on and around a tableland, standing ~30 m above the Coastal Plain, oriented ~N10°E, ~11 km long, and ~5 km wide, and considered as the most frontal structure of the mountain belt. Based on geomorphology, Quaternary geology, and gravity anomalies (Lin, 1969; Lin et al., 2000; Pan, 1968; Sun, 1964), the Tainan Tableland has long been recognized as an active anticline, probably fault related and bounded to the east by the Houchiali fault. The Holocene uplift rate was constrained to 5 mm/a based on stratigraphy and ^{14}C dating from boreholes (Chen and Liu, 2000). More recently, several geodetic surveys based on GPS, precise leveling, and Interferometric Synthetic Aperture Radar (InSAR) revealed rapid and transient deformation of the tableland, with uplift rates up to ~10–12 mm/a (Ching, Hsieh et al., 2011; Fruneau et al., 2001; Huang et al., 2006, 2009; Huang, Bürgmann, et al., 2016; Wu et al., 2013; CGS, 2014). Hence, the Tainan Tableland, which hosts ~1 million inhabitants, became an important focus for seismic hazard assessment. However, the geometry of the geological structures responsible for the tableland growth remains debated. Structural models include a diapiric fold underneath the tableland based on gravity anomalies (Hsieh, 1972; Pan, 1968), a fault-related fold associated to a west dipping thrust; a pop-up structure or more complex fault geometries, based on geomorphology, outcrops, InSAR, or seismic reflection profiles (Fruneau et al., 2001; Huang et al., 2004; Huang et al., 2009; Lacombe et al., 1999; Lee, 2003; Sun, 1964); and an east dipping normal fault based on shallow seismic reflection profiles (Kuo, 1999).

In this study, we investigate the subsurface structure, the mechanism of growth, and the deformation history of the Tainan anticline. We first interpret and analyze depth-converted seismic reflection profiles located north of the tableland to determine the fold geometry and mechanism of growth, to constrain the total shortening and to estimate the timing of fold inception. We also determine the Holocene shortening rate across the tableland based on a shallow borehole data set. Next, we use topography and surface deformation observed by InSAR on and around the tableland to infer a fold model beneath the tableland and estimate the cumulative shortening in the central part of the fold. At last, we discuss the implications of our results for the regional tectonics and for seismic hazard assessment.
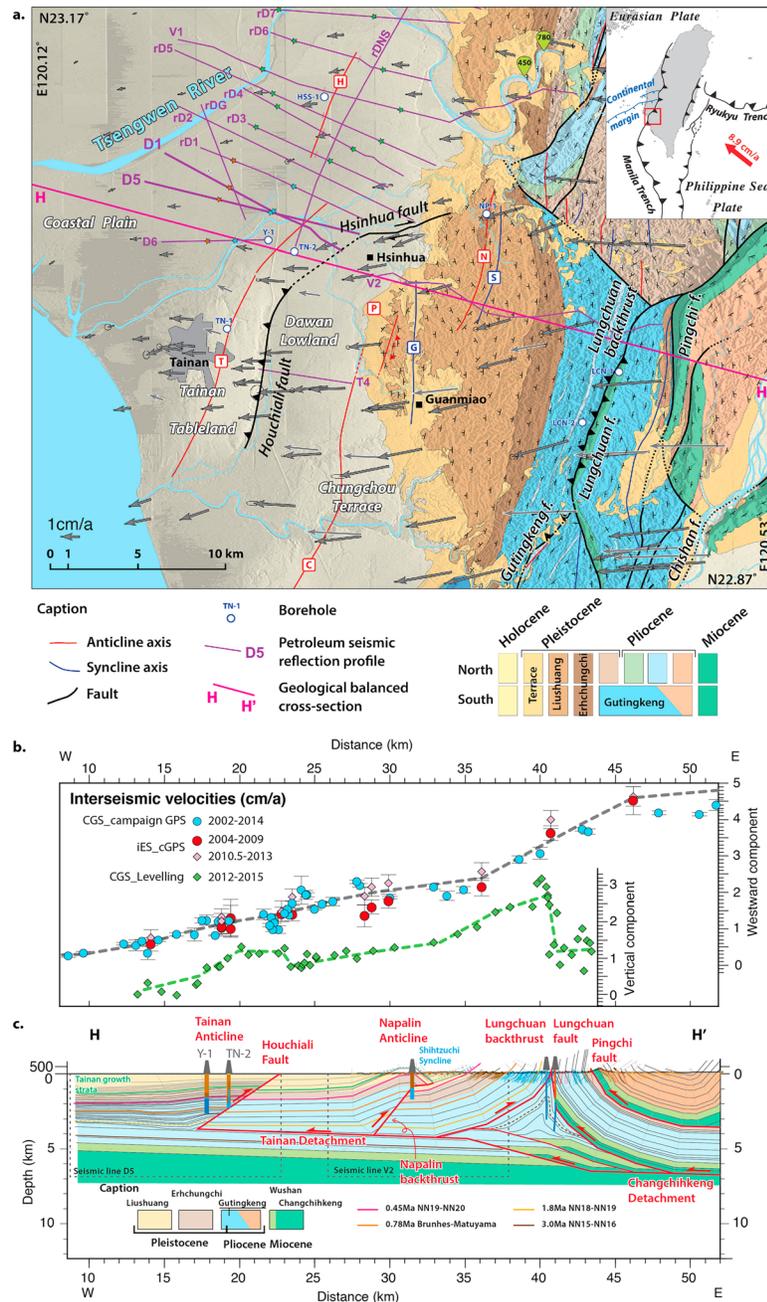
Figure 1. (a) Regional geological map of Tainan area, southwestern Taiwan, modified from Chinese Petroleum Corporation 1:100,000 map, Tainan sheet (1989). Fold axes: T = Tainan anticline; C = Chungchou anticline; H = Hsinying anticline; P = Pitou anticline; N = Napalin anticline; G = Guanmiao syncline; S = Shihtzuchi syncline. Axes of Tainan and Chungchou anticlines are inferred from Pan (1968) Bouguer gravity anomaly map. Orange and blue stars correspond to axial surfaces mapped from the seismic lines (color code similar to fold schematic model on Figure 2); Green stars bound the Hsinying detachment fold, based on the seismic lines. Horizontal GPS velocities are from the Central Geological Survey (CGS) (2014), with white and black arrows corresponding to continuous and campaign stations, respectively. Inset map shows the background tectonic setting: Taiwan lies at the convergent boundary between the Luzon volcanic arc on the Philippine Sea plate and the continental margin of the Eurasia plate (Suppe, 1984). The main normal faults of the passive margin are from Lin et al. (2003) and Yang et al. (2016). Plate convergence rate is from Argus et al. (2011). (b) Present-day crustal deformation across the Western Foothills of southern Taiwan (Transect HH′): westward and vertical velocities based on GPS and leveling (Central Geological Survey, 2014). (c) Balanced cross-section HH′ modified from Le Béon et al. (2017). The Tainan Anticline is the most frontal structure of a fold-and-thrust belt that includes a series of three back thrusts. The Tainan Detachment likely extends 15 km eastward from the Tainan Anticline, where it steps down to a deeper stratigraphic horizon within the Miocene Changchihkeng formation.

2. Subsurface Structure of the Tainan Anticline North of the Tableland

2.1. Data: Seismic Reflection Profiles and Chronological Constraints

To investigate the geological structure beneath the Tainan Tableland, we use two deep seismic reflection profiles, D1 and D5, located in the Coastal Plain immediately to the north of the tableland (Figure 1a). The two seismic lines intersect each other, so that similar geological structure and sediment properties are expected. Line D1 was previously interpreted regarding regional geology based on a two-way travel-time vertical axis (Huang et al., 2004). In this study, we present detailed interpretation and analysis, layer by layer, of Seismic Lines D1 and D5. Both lines were depth-converted based on Lieske (2000), using a simple velocity model based on the stacking velocities estimated during the seismic line processing (Figures S1 and S2 in the supporting information). Additional seismic lines located in the Coastal Plain and in the foothills (Figure 1a) were used based on the two-way travel-time vertical axis to constrain the larger-scale structural context and to establish correlations between deep sedimentary horizons and the surface geology.

Geochronological constraints from the literature were compiled and incorporated into this study in order to constrain the deformation history and to bring the reflectors imaged in the seismic lines into the sedimentological context of the Chinese passive continental margin and foreland basin development in southwestern Taiwan. The post-Miocene geological formations in the Western Foothills represent the filling sequence of the Taiwan foreland basin. The basin developed over the precollisional outer continental shelf to continental slope transition, extending from a deep marine environment during the deposition of the Plio-Pleistocene Gutingkeng mudstone (~0.8–3.5 Ma) to the shallow marine Erchungchi formation (~0.5–0.8 Ma) and the lagoonal to continental Liushuang formation (<0.5 Ma; Chi, 1978; Chen et al., 2001; Covey, 1984a, 1984b, 1986; Horng and Shea, 1994; Mouthereau et al., 2001; Figure 1). Biostratigraphic data based on nannofossils show strong lateral facies variations during the Pleistocene, with shallow marine to continental environments in the east and north, while mudstones characteristic of a deeper environment were deposited in the west and south. Therefore, formation boundaries cannot be used as age constraints, and it is difficult to correlate Coastal Plain borehole strata with formations in the foothills. In the following, we consider absolute age constraints as anchor points and use similar formation names to horizons in the foothills that lie along the same mapped seismic horizons, even though lithofacies may be muddier within the Tainan anticline.

Age constraints come from magnetostratigraphy and nannostratigraphy along the Tsengwen River section of the Western Foothills (Chen et al., 2001; Chi, 1978; Horng, 1991) and from nannostratigraphy within borehole HSS-1 (Wu et al., 1993; Figure 1). Constraints from outcrops in the foothills can be projected onto Seismic Line V1 using bedding strike data from the surface geology. Only the strata dated at 450 ka (NN19-NN20 transition) and at 780 ka (Brunhes-Matuyama magnetic reversal) could be matched with well-imaged reflectors. The nannofossil transitions NN18-NN19 (1.8 Ma), NN15-NN16 (3 Ma), and NN12-NN13 (5 Ma) come from borehole HSS-1, drilled along Seismic Line V1. Then, following the well-imaged reflectors from Seismic Lines V1, rDNS, rD1, rD2, and rDG (Figure 1a), the four dated horizons could be carried into Seismic Lines D1 and D5 (Figures 2 and S3). The depth of the transitions NN18-NN19 and NN15-NN16 is less well constrained because they lie within packages of unconformable strata of variable thicknesses, also affected by channeling.

2.2. Stratigraphic and Structural Interpretation of the Seismic Profiles

Above ~3.5-km depth, we generally observe fairly continuous reflectors that are subhorizontal on the western part of the profiles, gently dip westward in the central part and are subhorizontal again to the east (Figures 2 and S3). This geometry corresponds to the west limb of the Tainan anticline, where the continuity of most reflectors indicates that there is no frontal east dipping thrust west of the fold. Between 2.5- and 3.5-km depth, some of the reflectors are cut by channel incisions (best seen on D5; Figure 2). At the eastern extremity of both seismic lines, reflectors are less well imaged. There is evidence for subhorizontal reflecting segments, with no clear indications of an eastward dip, and a lack of continuity with the folded reflectors to the west. Besides, the point where each folded reflector becomes discontinuous or indistinct appears shifted to the west with increasing depth, delineating a ~35°W dipping back thrust bounding the fold to the east. The stratigraphic correlation across the fold results from the eastward extrapolation of the undeformed reflectors imaged on the west part of the seismic lines, considering their dip as the regional bedding dip. Looking now
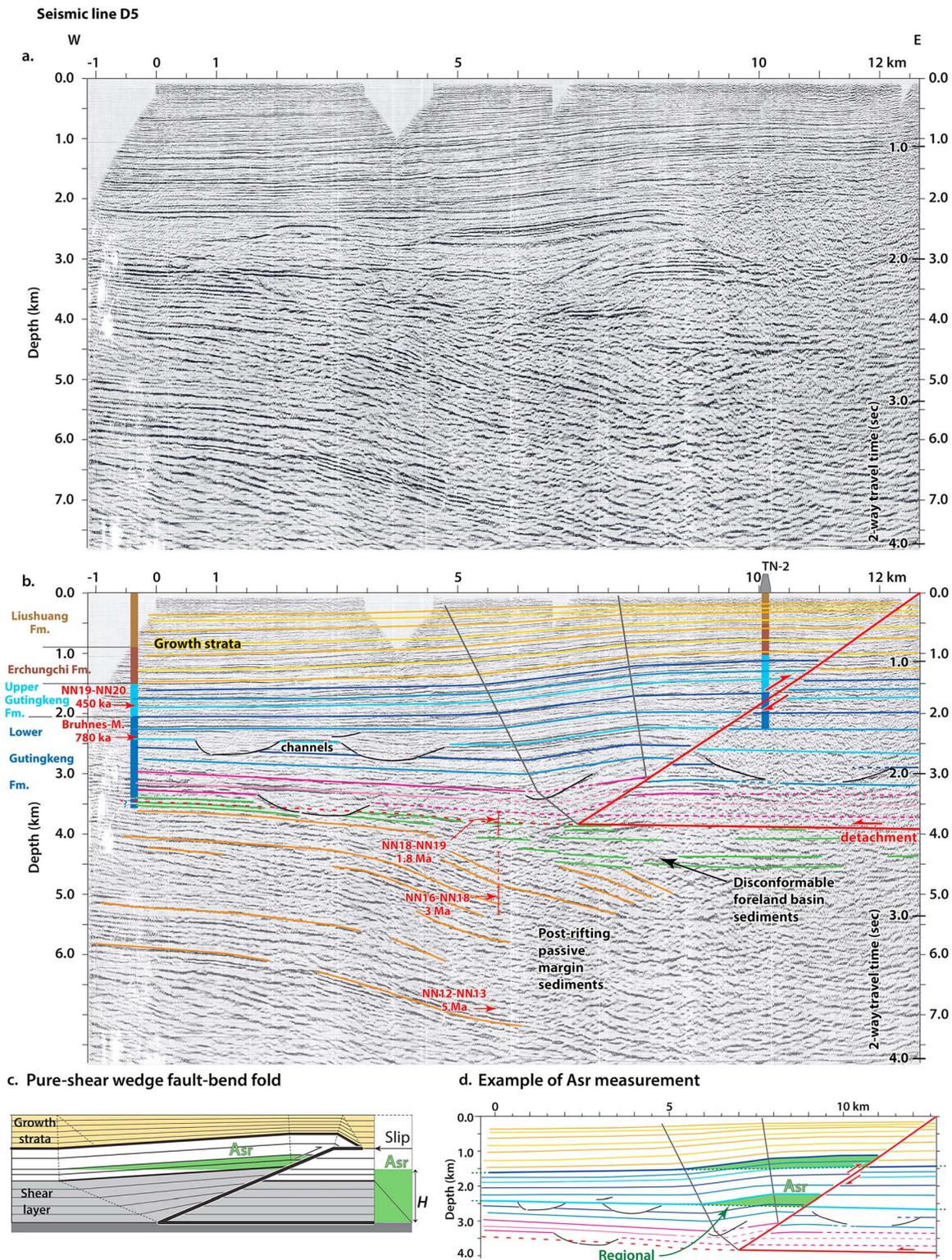
Figure 2. Seismic reflection profile D5 (a) without interpretation and (b) with mapped reflectors and the structural interpretation. The reference depth corresponds to the ground surface, equivalent to 0–5 m above sea level. TN-2 borehole stratigraphy is from Yuan (1987), with colors following caption on Figure 1 (dark blue = Lower Gutingkeng formation). Age constraints are from Chi (1978), Wu et al. (1993), Horng (1991), and Chen et al. (2001; see text for more details). (c) Conceptual toy model of a pure-shear fault-bend fold growing above a back thrust (Suppe et al., 2004; modified after Yue et al., 2011). The area of structural relief A_{sr} (green area) of a given strata lying at a height H above the detachment is equivalent to the product of shortening and H. (d) Example of A_{sr} measurement on seismic line D5.

in more details at the fold limb, we observe that reflectors from ~1.5- to ~3.0-km depth have similar dips of 7–8°W, while the deeper reflectors appear to be steeper (best seen on D5; Figure 2), and the shallower reflectors show gradually decreasing dips toward the surface. The fold limb dips are shallower than the dip of the inferred back thrust.

We interpret the folded reflectors imaged in these seismic lines as a shear fault-bend fold resulting from the westward propagation of a structural wedge or triangle zone, delimited by a west dipping back thrust rooted on a subhorizontal detachment (Suppe et al., 2004; Figures 2c and S4). The back thrust geometry is inferred from the reflector discontinuities while attempting to follow them eastward. While the back thrust is not clearly observed within the upper 1 km, the lack of evidence for an east dipping fold limb (east dipping reflections or poor imaging due to steep dips) motivates drawing a constant-dip fault all the way to the near surface, instead of a buried fault tip or a fault that is flattening within the growth strata (Figure S4). The apparent dips of the back thrust on both lines lead to a back thrust strike of N44°E and a true dip of 38°W. The detachment depth is estimated from the transition between undeformed and folded reflectors, which lies between 3.5- and 3.9-km depth near the wedge tip. Further analysis of the reflectors presented in section 3 will help better constrain the detachment depth. The detachment lies within the Lower Gutingkeng mudstone, near the NN18–NN19 transition dated at 1.8 Ma (Figure 2b), and is expected to follow the regional bedding dip, in the order of 2°E. The geometry of the west limb, with fold limb dips lower than the back thrust dip, points to a shear fault-bend fold that grows by progressive limb rotation above a basal shear layer (Corredor et al., 2005; Shaw et al., 2005; Suppe et al., 2004). In contrast, the fold limb of a classical fault-bend fold displays similar dips to the fault ramp due to folding by kink-band migration (Shaw et al., 2005; Suppe, 1983; Suppe et al., 1992; Figure S4a). Limb rotation is also indicated by the gradually decreasing dips of the shallower reflectors toward the surface. This is a characteristic of syntectonic sediments called "growth strata," the base of which marks the onset of folding (Gonzalez-Mieres and Suppe, 2011; Shaw et al., 2005; Suppe et al., 1992; Figure S4). The observed fold limb geometry could relate to either pure-shear or simple-shear fault-bend folding in the case of forward thrusts, but only to pure-shear fault-bend folds in the case of back thrusts (see Suppe et al., 2004; Figure S4). Indeed, as expected from the pure-shear model that is characterized by thickening of the basal shear layer, reflectors within the fold core display steeper dips than that of the intermediate-depth reflectors, and the dip of the syncline axial surface is steep (64–76°) from the surface down to ~3.2-km depth and becomes shallower (~40°) within the basal shear layer (Figures 2 and S3). The fold models in Figures 2c and S4b consider folding only from flexure above the ramp and shear layer. We will show in section 3 that the upper layers have also undergone some pure shear.

Similarly to Lines D1 and D5, Seismic Lines D6 and rD1, located, respectively, ~3 km south and ~2 km north of D1 and D5 (Figure 1a), also show continuous reflectors in the upper part of the profile, which are subhorizontal on the west part, gently west dipping in the central part, and subhorizontal again in the east part. The locations of the syncline and anticline axial surfaces in map view are consistent with the location of the fold limb observed on D1 and D5 (Figure 1a). These lines do not bring additional observations regarding the wedge structure. For D6, in spite of limited reflections below 2.0 s, the fold seems to affect a similar stratigraphic thickness to D1 and D5. The deepest deformed reflector we could identify lies at 2.1 s, equivalent to 3.3-km depth assuming a similar velocity structure to D1 and D5, and the shallowest undeformed reflector is seen at 2.3 s, equivalent to 3.8-km depth. For rD1, low-quality imaging below 1.8 s only allows constraining the detachment depth to 1.8 s or deeper. Line rD2, ~2 km north of rD1 (Figure 1a), only exhibits subtle folding, strongly suggesting that the Tainan anticline has vanished at this latitude.

Below ~3.5-km depth on Lines D1 and D5, we observe reflectors that gently dip to the east in the western part of the lines and which dip increases in the central part of the lines (Figures 2 and S3). They are unconformably overlapped by a series of subhorizontal reflectors that decrease in total thickness westward. The east dipping reflectors dated between 5 and 2–3 Ma are likely to correspond to postrifting sediments from the Chinese passive continental margin, overlapped by what could be the first foreland basin sediments that are dated at 2–3 Ma and coming from the erosion of the growing Taiwan orogen, which was further to the northeast at that time. The channels observed between ~3.5- and ~2.5-km depth may correspond to submarine canyons incised within the continental slope during low sea level stands. The significant incisions prior to Brunhes-Matuyama reversal (780 ka) might be related to the glacial periods Marine Isotope Stage 20 dated at 790–810 ka or Marine Isotope Stage 22 (870–900 ka; Lisiecki and Raymo, 2005).

3. Mechanisms of Shortening

3.1. Determination of Structural Relief Shortening and Detachment Depth

3.1.1. Principle of the Area of Structural Relief Analysis

The mapped reflectors can be used to analyze the area of structural relief as a function of depth, or height above the detachment, in order to constrain the amount of shortening consumed in the fold and the detachment depth (Eichelberger et al., 2017; Epard and Groshong, 1993, 1995; Gonzalez-Mieres and Suppe, 2006, 2011; Groshong, 2015; Wang et al., 2018). This technique, also called area-height or area-depth analysis, assumes that areas are conserved within an observed cross section (i.e., no material flowing in or out of the section plane during deformation). Additional deformation may be associated with changes in area, for example, due to horizontal compaction (Gonzalez-Mieres & Suppe, 2006), as discussed in section 3.2. For each geological stratum, the area of structural relief A_{sr} comprised between the stratum and the regional, nondeformed, initial stratigraphic level is equal to the area defined by the horizontal shortening on the detachment and the height H of the layer above the detachment (Figure 2c). Therefore, considering a series of reflectors, the areas of structural relief plotted as a function of the reflectors height above the detachment can be fitted by a regression line, which slope corresponds to the mean shortening S_{sr} experienced by the layers. We can also determine the bed-by-bed structural shortening at any depth z, $S^*(z) = dA_{sr}(z)/dH(z)$. The difference between the two shortening values, if any, may provide additional information regarding the fold mechanical behavior, such as a contribution of simple shear (Gonzalez-Mieres and Suppe, 2006; Hubert-Ferrari et al., 2007). The area-depth analysis applies to any kind of fold, regardless of the fold structural model and growth mechanism.

The area of structural relief A_{sr} associated to growth strata reflectors departs from the linear trend defined by pregrowth reflectors: A_{sr} increases less rapidly or even decreases with the height above detachment, depending on the ratio between shortening rate and sedimentation rate (Gonzalez-Mieres and Suppe, 2011; Groshong, 2015; Hubert-Ferrari et al., 2005, 2007; Schlische et al., 2014). Therefore, the area-depth graph allows us to constrain the depth of the base of the growth strata more precisely than visual observation of the seismic line and to discuss the ratio between sedimentation and shortening during the fold growth. If the layers within the growth strata can be dated, the timing of the fold inception can be determined, as well as the shortening rate evolution with time.

3.1.2. Methods and Results

In this study, the area-depth analysis follows the method of Eichelberger et al. (2017), applicable to structures controlled by faults that cut and displace the geological strata. We used the back thrust geometry and the reflectors mapped on Figures 2 and S3, slightly modified to interpolate across the channel incisions (Figure 2d). The footwall reflectors were extrapolated from the regional dip as observed west of the fold, neglecting the uplift due to translation on a dipping detachment and the small angle between the detachment and the regionals (Wang et al., 2018). The area of structural relief depends significantly on the reflector depth in the footwall, which depends on the regional dip. To estimate this uncertainty, we considered for each reflector the shallowest and steepest regional dip that fitted the reflector on the western part of the lines, and, in turn, we modified the height of the corresponding layer on the footwall and computed the A_{sr}. We found uncertainties in the order of 3–7% for most reflectors, increasing to 13% for irregular or less well-imaged reflectors. The mean shortening S_{sr} and detachment depth were determined by least squares linear regressions through the A_{sr} and depth z data sets, considering the data sets from D1 and D5 separately or combining them, and including or excluding reflectors that may or may not belong to the growth strata. We ignored the deepest reflectors involved in the fold due to poor imaging. The best fits that we obtained provided consistent results no matter D1 and D5 data sets were considered separately or combined. We favor the result obtained from the combined data sets (Figure 3a).

In Figure 3a, the areas of structural relief A_{sr} associated to D1 and D5 reflectors increase linearly from ~2.9- to ~1.5-km depth. Above ~1.5-km depth, A_{sr} values depart from this trend, as expected for growth strata, and they decrease rapidly, indicating a sedimentation rate significantly faster than the shortening rate (Gonzalez-Mieres and Suppe, 2011). Least squares linear regression through the pregrowth data set gives a mean shortening S_{sr} of 529 $\pm$ 44 m (2σ) along the direction N104°E, that is, the orientation of D5, and a detachment depth of 3,830 $\pm$ 140 m (2σ). This depth serves as a reference to compute the heights H above the detachment. Assuming that the mean orientation of GPS velocities in Tainan area, which is ~E-W
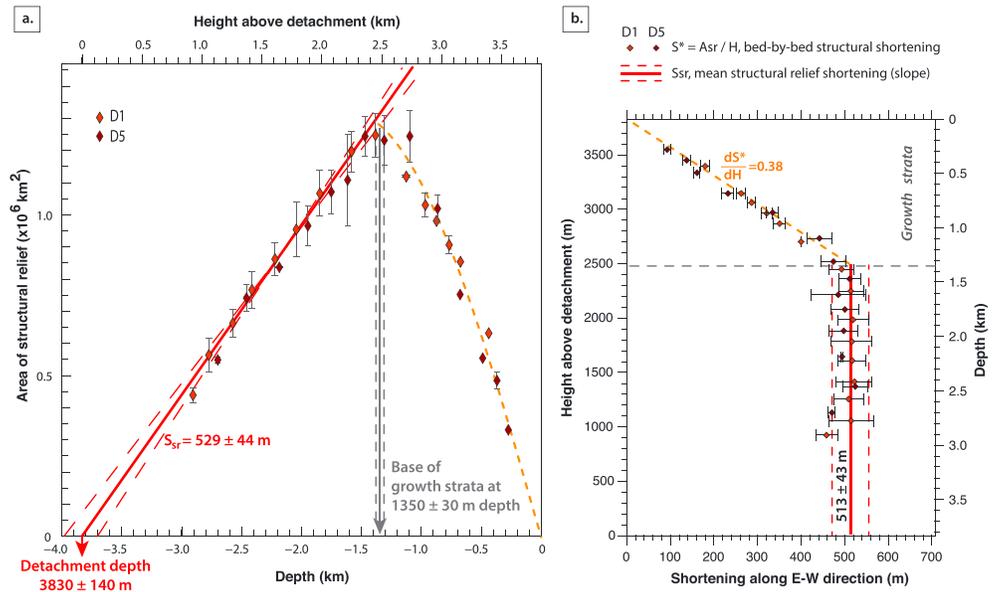
Figure 3. (a) Area of structural relief A_{sr} as a function of reflector depth and height H above the detachment for Seismic Lines D1 and D5. Least squares linear regression constrains the mean shortening S_{sr} along N104°E (the orientation of D5) and the detachment depth. Least squares regressions also helped determine which reflectors belong to pregrowth strata or growth strata. (b) Structural shortening depth-profile along the E-W direction. Bed-by-bed structural shortening S^* values are computed from A_{sr} and H values for each reflector. The mean structural shortening S_{sr} of 513 ± 43 m corresponds to the shortening determined from the slope of the area-of-relief graph (a), projected on the E-W direction. Growth strata reflectors suggest a simple growth history with a larger sedimentation rate than the shortening rate ($dS/dH = 0.38$).

(Figure 1a; Ching, Rau, et al., 2011; CGS, 2014; Tsai et al., 2015), is representative of the long-term shortening direction, we project the mean shortening determined along the direction N104°E onto the E-W direction, and we obtain a mean shortening S_{sr} of 513 ± 43 m. The base of the growth strata is determined at $1,350 \pm 30$ m depth. It is bracketed by the shallowest reflector that is consistent with the best fit linear regression and by the deepest reflector that departs from this linear regression. The shortening depth profile (Figure 3b) is computed from the bed-by-bed area-of-relief values and heights and projected on the E-W direction. It shows a constant trend within the pregrowth strata, representative of the linear increase in Figure 3a. The growth history appears to be fairly simple, with S^* values linearly decreasing with depth, with a constant shortening rate over sedimentation rate ratio of 0.38. Accounting for uncertainties in the velocity model used for depth conversion (Figures S1 and S2), the depth ranges become $3,830 \pm 400$ m for the detachment and $1,350 \pm 90$ m for the base of the growth strata. Because the fold is wide with a low relief, the effect of uncertainties in the velocity model on the structural shortening remains negligible.

Theoretical geometric relationships were established for pure-shear fault-bend folds between fault dip, fold limb dip, shear layer thickness h, and total shortening i (Suppe et al., 2004). For a 38° fault dip, a 9° true dip for the fold limb, and a 560-m-thick basal shear layer, the model predicts a syncline axial surface dipping 36°E within the basal shear layer (fairly consistent with the 37° and 40° values estimated from D5 and D1, respectively) and a fault-perpendicular shortening of 390 m. This shortening value corresponds to an E-W shortening of 560 m, in good agreement with the mean E-W structural shortening of 513 ± 43 m that we obtained. Therefore, the observed fold geometry matches reasonably well the simple theoretical model.

3.2. Components of Shortening and Total Shortening
3.2.1. Curvimetric Shortening
The curvimetric (or bed-length) shortening S_c is traditionally used to quantify shortening by measuring the difference between the curvimetric length of a deformed bed and the length of an undeformed bed following
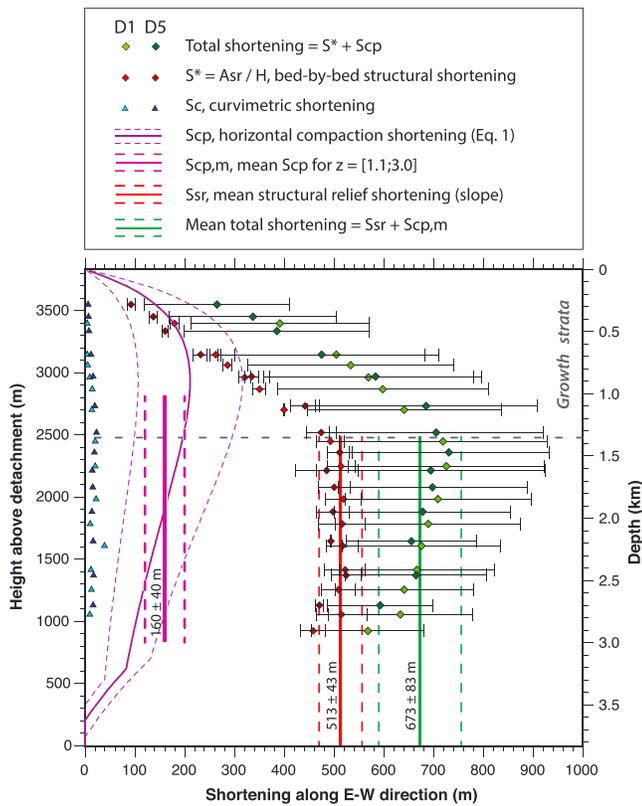
Figure 4. Evolution of the different components of shortening along the E-W direction (the mean orientation of GPS velocities) with height above the detachment and depth. The bed-by-bed structural shortening S^* is calculated from the A_{sr} and H values associated to each reflector. S_{sr} is the mean shortening determined from the area of structural relief analysis, that is, the slope of Figure 3 graph. The horizontal compaction shortening S_{cp} is estimated from the difference in the porosity-depth profiles within the fold and west of the fold (equation (1); Figure 5; see text).

the regional dip between the same end points, under the assumption that bed length is conserved during folding (Laubscher, 1961; Gonzalez-Mieres and Suppe, 2006). The comparison of curvimetric shortening and structural relief shortening allows testing the bed-length conservation assumption and determining if shortening is consumed mainly by flexure or by shear (Gonzalez-Mieres and Suppe, 2006; Yue et al., 2011). In this study, for both seismic lines, S_c is only in the order of 15–20 m (Figure 4), which represents only 2–4% of S_{sr} and shows that flexure is negligible. This value is discussed in section 3.2.3, together with the other components of shortening.

3.2.2. Horizontal Compaction Shortening

Gonzalez-Mieres and Suppe (2006) showed that horizontal compaction could be a significant and even dominant mechanism in accommodating shortening across the frontal structures of fold-and-thrust belts, mainly based on examples from the Cascadia and Nankai accretionary prisms. To investigate the contribution of horizontal compaction in Tainan area, we used the stacking velocities along Seismic Lines D1, D5, and D6 (Figure 1) to estimate the vertical gradient in compaction within the fold and west of the syncline axial surface. We converted the stacking velocities into density using empirical relationships for terrigenous sediments (Hamilton, 1978). We then introduced compaction through porosity Φ using the equation $\rho = \rho_s (1-\Phi) + \Phi*\rho_w$ with ρ the bulk density, ρ_s the sediment grain density ($\rho_s = 2.7$ g/cm^3), and ρ_w the water density. The data were separated according to shot point location, on one hand those located between the syncline axial surface and the fault trace, considered within the fold, and on the other hand those located west of the syncline axial surface, that is, out of the fold. Porosity decreases relatively rapidly with depth, from 44–46% in the near surface, in agreement with independent porosity measurements (Wang et al., 2015), to 2–3% at 3.5-km depth (Figure 5), illustrating the increase in vertical compaction due to sediment overburden. While drilling TN-1 borehole (Figure 1), the mud weight had to be significantly increased at ~3.0-km depth (Huang et al., 2004), which indicates higher pore fluid pressure and likely corresponds to the fluid

retention depth, which is typically ~3 km in western Taiwan (Yue & Suppe, 2014). Below this depth, sediments reached a maximum in compaction, so that incremental sedimentary or tectonic load is supported by pore fluid instead of compaction (Suppe, 2014). We fitted exponential decays through the porosity data located within the fold and out of the fold for Lines D1 and D5 combined together, and for Line D6, fixing the surface porosity to 48%.

Although the porosity estimates are scattered, the least squares fits show that porosity decreases more rapidly with depth within the fold than out of the fold (Figure 5). Further statistical examination of the significance of the difference between the two data sets using a Mann-Whitney U test led to probabilities of 94% or higher that porosities inside and outside the fold are different for depths of 0.5 to 2.0 km, with systematic lower values inside the fold compared to outside (Figure S5). We explain this difference with horizontal compaction along the direction of shortening, considered E-W. We use the difference in porosity-depth profiles within the fold and out of the fold $\Delta\Phi(z)$ as a proxy to estimate the horizontal compaction shortening S_{cp} based on equation (1):

$$S_{cp}(z) = \frac{L_0 \Delta\Phi(z)}{1 - \Phi_f(z)},$$

(1)

where L_0 is the initial length of the undeformed layers, taken as the fold width in the near surface, considered constant and equal to 8 km. $\Phi_f(z)$ corresponds to the final porosity (i.e., the best fit porosity-depth profile within the fold). Potential variations in horizontal compaction from layer to layer cannot be assessed here and are neglected.
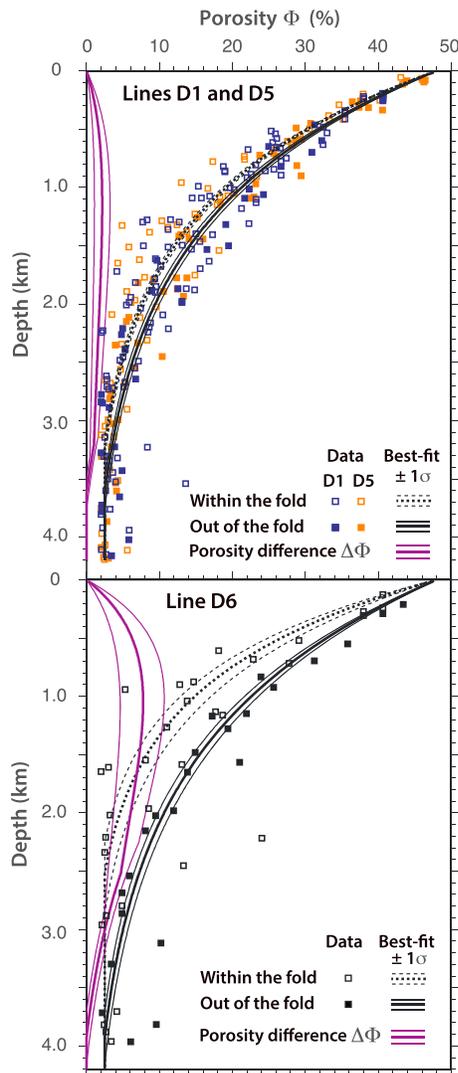
Figure 5. Porosity Φ (derived from stacking velocities) against depth for seismic reflection profiles D1 and D5, and D6. Velocity-depth profiles were separated in two groups based on shot point location: within the fold (solid squares), for shot points located between the fault and the syncline axial surface, and out of the fold (open squares), for shot points located west of the syncline axial surface. Porosity data sets were fitted with an exponential decay with depth, imposing a surface porosity of 48%, and using an iteratively reweighted least squares robust fit (Holland & Welsch, 1977; Dumouchel & O'Brien, 1991). The best fits were subtracted to obtain the porosity difference $\Delta\Phi$ used to determine the contribution of horizontal compaction to shortening (Figure 4). Statistical examination of porosities in and out of the fold shows that the data set is significantly different (probability $\geq94\%$) from depths of 0.5 to 2.0 km (Figure S5).

Both for D1 and D5 and for D6, the horizontal compaction shortening S_{cp} rapidly increases from the surface to ~1.0-km depth (Figure 5), as expected from growth strata. The maximum porosity difference for the D1 and D5 data set is 2.1 ± 1.1 % (2σ), which corresponds to 210 ± 100 m for S_{cp}. Along Line D6, the maximum porosity difference is significantly larger, reaching 7.8 ± 3.0% (2σ), which corresponds to 720 ± 280 m for S_{cp}. From ~1.0-km to ~2.4- to 3.0-km depth, S_{cp} slowly decreases with depth, until it decreases rapidly as the sediments start to reach maximum compaction near the fluid retention depth. The progressive decrease in $\Delta\Phi$ and S_{cp} between ~1.0-km and ~2.4- to 3.0-km depth is hard to explain geologically. It may be an artifact of our simple porosity-depth model or due to sediments heterogeneity. We would rather expect a constant porosity difference within this depth range. Therefore, we approximate the progressive decrease by a constant by computing the average and standard deviation of $S_{cp}(z)$ for z = [1.1; 3.0 km] for D1 and D5 and z = [1.0; 2.4 km] for D6. We obtain an average horizontal compaction shortening $S_{cp,m}$ in the E-W direction of 160 ± 40 m along D1 and D5 and 580 ± 100 m along D6. These values are minimum estimates, as our data set is located at most 5 km away from the fold, while the increase in seismic velocities interpreted as horizontal compaction was observed at 6–8 km away from the deformation front at the Cascadia and Nankai accretionary prisms (Bangs and Gulick, 2005; Cochrane et al., 1994).

3.2.3. Shortening Components and Total Shortening

Figure 4 synthesizes the different components of E-W shortening determined from Seismic Lines D1 and D5: shortening determined from the structural relief analysis (mean structural shortening S_{sr} and bed-by-bed structural shortening S^*; Figure 3), the inferred minimum horizontal compaction shortening (S_{cp}, computed from equation (1) and $S_{cp,m}$, the average for z = [1.1; 3.0 km]), and the curvimetric shortening S_c. We estimate the total shortening by adding the mean horizontal compaction shortening estimate ($S_{cp,m}$ = 160 ± 40 m) to the mean structural relief shortening (S_{sr} = 513 ± 43 m). We obtain a total shortening of 673 ± 83 m. Horizontal compaction accounts for 24% of the total shortening. The horizontal compaction shortening may be larger if horizontal compaction extends further west than the 5-km distance covered by our data set. The curvimetric shortening, of the order of 15–20 m, represents only 2–3% of the total shortening. This indicates negligible flexure, meaning that most of the deformation is related to shear through layer-parallel thickening and horizontal compaction (Gonzalez-Mieres and Suppe, 2006), in agreement with the fold model that we proposed.

Along line D6, we inferred a horizontal compaction shortening of 580 ± 100 m. This component alone is in the order of the total shortening along D1 and D5. This strongly suggests that the total shortening increases southward, toward the Tainan Tableland.

4. Sedimentation and Deformation History

Now that we determined the cumulative shortening at the latitude of Seismic Lines D1 and D5, we use the geochronological constraints that we carried into the seismic lines (see section 2.1) to estimate sedimentation rates during the Middle to Late Pleistocene, and then the timing of the beginning of fold growth and the long-term shortening rate at the latitude of the seismic lines. Next, we also examine available data on the Holocene stratigraphy that could allow us to constrain the Holocene shortening rate.

4.1. Middle to Late Pleistocene Sedimentation Rates

To estimate the sedimentation rates since 780 ka and the sediment thickness deposited since the beginning of fold growth, we first corrected for the vertical compaction of the sediments. Equation (2) represents the decompacted thickness, $H_d(z)$, of a layer at any given depth, assuming its original porosity was equal to the modern surface porosity:

$$H_d(z) = H(z)\frac{1-\Phi(z)}{(1-\Phi(0))} \tag{2}$$

with $\Phi(0) = 48\%$ and $\Phi(z)$ taken as the best fit porosity-depth profile west of the fold for Seismic Lines D1 and D5 (Figure 5). To account for vertical compaction at any depth z, we consider the cumulative sum of the vertical compaction term from the surface to the depth z. For the base of the growth strata at $1,350 \pm 90$ m depth, for the 450-ka reflector at $1,760 \pm 180$ m depth, and for the 780-ka reflector at $2,300 \pm 190$ m depth, respectively, we obtain decompacted sediment thicknesses of $1,855 \pm 120$ m, $2,550 \pm 271$ m, and $3,475 \pm 300$ m. Note that the depth uncertainties include the uncertainties related to depth location on the seismic lines and to time-depth conversion.

Radiocarbon ages from shallow wells around the Tainan Tableland (Chen and Liu, 2000; Lu, 2006) indicate a rapid sedimentation rate of 11 ± 1 mm/a for the last ~12 ka. Accounting for this Holocene sedimentation rate, we obtain a mean sedimentation rate of 5.5 ± 0.6 mm/a from 12 to 450 ka and a slower sedimentation rate of 2.8 ± 1.7 mm/a between 450 and 780 ka. These values compare well with the Late Pleistocene sedimentation rate of 3–5 mm/a between ~15 and ~45 ka determined from Lu (2006) and Chen et al. (2004) databases within the Coastal Plain, as well as with earlier studies in the foothills of Tainan that proposed sedimentation rate estimates of 1.5–3.0 mm/a during the Early to Late Pleistocene (0.45–2.0 Ma), increasing to 1.8–4.5 mm/a for the last 450 ka (Chang and Chi, 1983; Chen et al., 2001), as expected for the Coastal Plain to become the proximal part of the foreland basin.

4.2. Timing of Fold Inception and Long-Term Shortening Rate North of the Tableland

The base of the growth strata is shallower than the 450-ka reflector, meaning that folding initiated less than 450 ka ago. Assuming that the sedimentation rate remained constant at 5.5 ± 0.6 mm/a between 450 and 12 ka and accounting for a Holocene sedimentation rate of 11 mm/a, the age at the base of the growth strata is estimated at 310 ± 50 ka.

The age of fold inception corresponds to the time when the structural shortening component started to accumulate. The total shortening that we determined also includes the horizontal compaction component, but there is no constraint on when horizontal compaction began. The Cascadia and Nankai examples, where horizontal compaction was observed at 6–8 km ahead of the deformation front (Bangs and Gulick, 2005; Cochrane et al., 1994), show that horizontal compaction started earlier than folding. Therefore, we first use the structural shortening of 513 ± 43 m and obtain a long-term E-W shortening rate of 1.7 ± 0.4 mm/a at the latitude of Seismic Lines D1 and D5 that represents a minimum value. Now accounting for the horizontal compaction shortening, we obtain a shortening rate of 2.2 ± 0.6 mm/a that is probably overestimated.

4.3. Holocene Uplift and Shortening Rates at the Latitude of the Tableland

The Tainan Tableland and Dawan Lowland were standing under sea level during the Early to Middle Holocene (Chen and Liu, 2000; Chen et al., 2004; Lu, 2006), which enables to quantify the deformation at the Holocene timescale. Lithofacies analysis and radiocarbon dates within shallow wells on and around the tableland allow reconstructing the coastal paleo-environments and paleo-sea levels (Chen and Liu, 2000; Chen et al., 2004; Lu, 2006). In this study, we rely on a database from Chen et al. (2004; Table S1; Figure 6) that we use to calculate uplift and subsidence rates and to estimate the Holocene shortening rate across the tableland based on folded isochrones.

First, paleo-sea levels can be used to determine uplift and subsidence rates by comparison of their current elevations with the worldwide paleo-sea level elevations at the times of deposition. We refer to paleo-sea level curves from Fairbanks (1989), Bard et al. (1996), and Chappell and Polach (1991) based on observations from Barbados, Tahiti, and Papua New Guinea. Vertical compaction was neglected due to the shallow depth
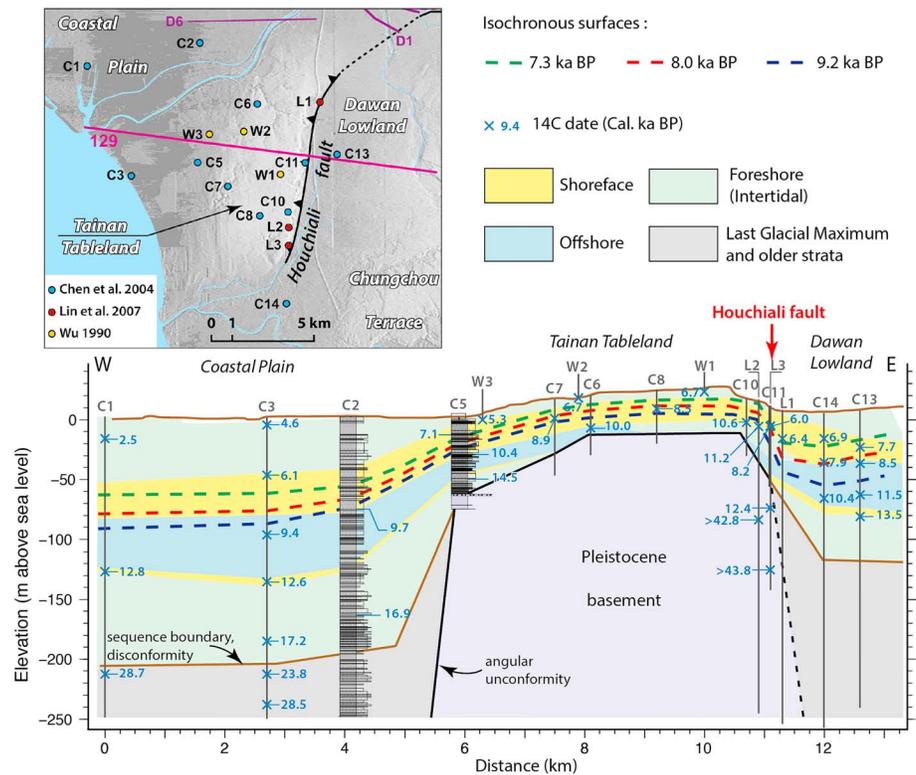
Figure 6. [14]C ages (Table S1) and sedimentary paleo-environments based on boreholes drilled on and around Tainan Tableland (Chen et al., 2004; C. W. Lin et al., 2007). Borehole data were projected on Transect 129. The age data and peculiar postglacial deposits were used to construct three isochrones that we used as strain markers to estimate the Holocene shortening rate.

range of the data and the lack of resolution of our porosity model for such depth range. Vertical decompaction would increase the depth of a layer lying at 100 m by only 4 m. Uplift and subsidence rates calculated for each dated layer are presented in Table S1. Within each tectonic domain, they vary within few millimeters per year, probably due to irregularities in the paleo-sea floor and possibly overestimated radiocarbon ages due to recycling of organic material. We computed an average subsidence rate of 4.9 ± 1.7 mm/a for the Coastal Plain and 1.4 ± 0.9 mm/a for the Dawan Lowland, and an average uplift rate of 3.8 ± 0.6 mm/a for the top part of the tableland (Table S1). These values are consistent with earlier estimates from Chen and Liu (2000). This leads to a Holocene uplift rate of 8.7 ± 2.3 mm/a of the tableland relative to the Coastal Plain. Provided a kinematic model of folding and a fold geometry that is valid at the latitude of the tableland, the uplift rate could be used to determine the shortening rate across the fold and/or the slip rate on the faults involved.

Second, Chen et al. (2004) database (Table S1) allows us to construct across the tableland isochronous surfaces representative of shoreface to foreshore environments at 7.3, 8.0, and 9.2 ka (Figure 6). These isochrones therefore represent proxies for paleo-sea level and can be used as strain markers. Similarly to folded reflectors, we can estimate their area of structural relief A_{sr} and then the bed-by-bed structural shortening S^* accommodated since their deposition (Gonzalez-Mieres & Suppe, 2006, 2011). We considered a subhorizontal regional, dipping 0.14–0.25°E, consistent with the present-day nearshore slope in the Taiwan Strait. For the 7.3-, 8.0-, and 9.2-ka isochrones, we obtain A_{sr} estimates of 0.276, 0.319, and 0.355 km^2, respectively. Given depths of 41 ± 10 m, 53 ± 10 m, and 65 ± 10 m, respectively, and the detachment depth of 3,830 ± 400 m, we obtain cumulative shortening estimates of 73 ± 8 m, 85 ± 9 m, and 94 ± 10 m. Linear regression through the shortening versus age data set yields a Holocene shortening rate estimate of 10.3 ± 1.0 mm/a (2σ) across the Tainan Tableland. This result is independent of the fold geometry and of any kinematic model of fold growth. It only relies on the detachment depth, considered to be similar beneath the tableland and north of it.

5. Relationship Between the Tainan Tableland and the Structures Imaged to the North

5.1. Approach, Data, and Method

This section aims at relating the fold geometry observed from subsurface imaging north of the topographic expression of the fold with the structure responsible for the growth of the Tainan Tableland. To do so, we relied on topography as a proxy for Holocene cumulative deformation and on present-day high-density surface displacement field imaged by InSAR during 1996–1999. The sharp deformation gradient observed across the eastern edge of the tableland during this period (Figure 7) is interpreted as aseismic slip along the Houchiali fault (Fruneau et al., 2001; Huang et al., 2006, 2009; Tung, 2008). The similarity of the present-day deformation pattern with topography, in map view and in section (Figure 7), suggests that it may represent permanent cumulative deformation and be due to aseismic slip on the entire Houchiali fault, downdip, and on the detachment. Thus, changes both in elevation gradient and in displacement gradient during 1996–1999 across the tableland would reflect the position of structural axial surfaces related to the subsurface geometry.

The interseismic surface displacements in Tainan are obtained from InSAR time series measurements during the period 1996–1999 using ERS satellites and based on a modified small baseline subset method as described in Huang, Bürgmann, et al. (2016). We generated a slant-range (SR) velocity map with 90-m pixel size (Figure 7a). The spatial consistency of the deformation field over the tableland and surroundings suggests that perturbations related to anthropogenic activities and groundwater were limited during this time period. This may not be the case to the north and northwest of the tableland that include industrial areas and fishponds with localized subsidence. Topography was analyzed using a 5-m DEM (Digital Earth Model) with 1-m accuracy on elevations. We extracted contour lines and swath profiles across the tableland and north of it with ≤1-km spacing.

5.2. Axial Surface Mapping Based on InSAR Velocity Field and Topography

Across the southern half of the tableland, axial surface mapping was quite straightforward (Figure 7). InSAR transects show a sharp gradient in SR velocity between the Dawan Lowland (Figure 1) and the tableland, which likely corresponds to the creeping Houchiali fault. This sharp gradient is collocated with the toe of the topographic scarp, commonly used to delineate the Houchiali fault trace (C. W. Lin et al., 2007). The anticline axial surface (light blue) is mapped at the transition between steady and fast (~8 mm/a) SR velocities on the tableland and continuously decreasing SR velocities further west, down to 0–2 mm/a within the Coastal Plain. In the topography, this axial surface corresponds to a change in slope, from a slightly west dipping (0.1–0.2°W) tableland to a 0.4–0.8°W slope on the west. The syncline axial surface (orange) is mapped mainly based on InSAR, where the westward decreasing SR velocities reach the background values within the Coastal Plain. Man-made modifications within the Coastal Plain prevent accurate mapping of the syncline axial surface based on topography. We consider that this axial surface would locate at the toe of the tableland or further west. To summarize, on the southern part of the tableland, axial surface mapping shows a fold oriented N5°E, with a wide fold crest and a narrower west limb, showing similar widths to the fold imaged in Seismic Lines D1 and D5 (Figure 2). InSAR transects show steady SR velocities on the tableland during 1996–1999. Although acquired during a different time period, we note that 2002–2014 GPS measurements (CGS, 2014) also show constant horizontal velocities on the tableland, which gently decrease further west (Figure 1). If the pattern of horizontal velocities were similar during 1996–1999, the uplift component would also be constant on the tableland and gently decreasing further west. This uplift pattern corresponds very well to the theoretical cumulative uplift transect expected from a pure-shear fault-bend fold (Yue et al., 2011; Figure S4).

Across the northern part of the tableland, axial surface mapping based on InSAR SR velocity could be pursued with confidence until ~1 km south of Seismic Line D6 (Figure 7a). It shows a clear change in the fold orientation from N5°E to N40–45°E, also visible from topography at the tableland eastern edge. The SR velocity gradient across the Houchiali fault becomes smoother there, as if coupling on the fault was stronger than to the south. Topography could not be used to map axial surfaces with confidence because of limited preservation of the morphology due to regressive erosion and remodeling of the Yenshui River banks. Further north of the change in azimuth of the fold, the InSAR SR velocity pattern changes completely, with velocities decreasing northward, as the fold topographic expression also dies out. The SR velocity gradient across what
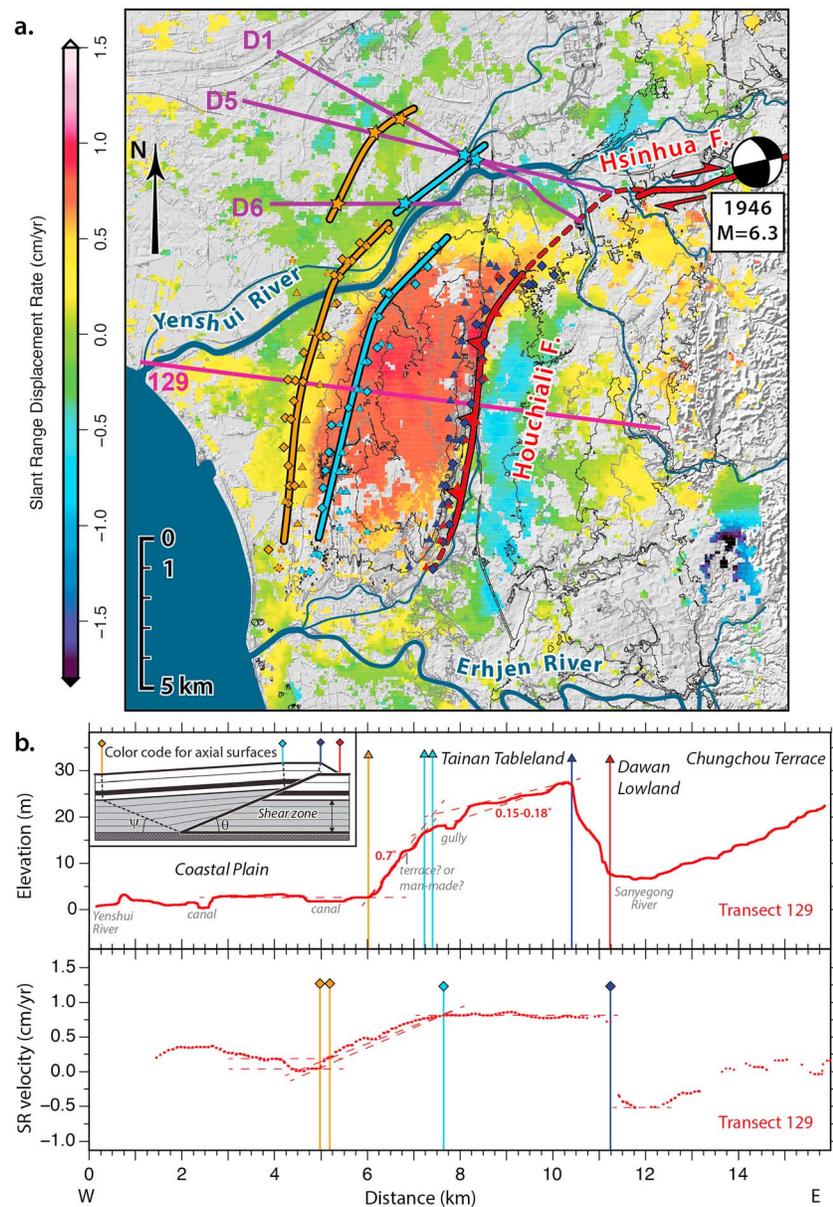
Figure 7. (a) Axial surface map based on Interferometric Synthetic Aperture Radar (InSAR) slant-range (SR) velocity field during 1996–1999 (diamonds), topography (5 m DEM; triangles) and seismic reflection profiles (stars; purple lines). Symbol color code is indicated on shear fault-bend fold schematic model on Figure 6b. Contour lines show elevation with 5-m interval. Background shows InSAR SR velocity field (Huang, Bürgmann, et al., 2016) over shaded topography. Satellite view angle is 23.5° in the direction N80°W (descending orbit). Location of Transect 129 (Figure 6b) is shown in purple. (b) Identification of axial surfaces based on topography and InSAR SR velocity along Transect 129.

would be the northward continuation of the Houchiali fault disappears, possibly because the fault-related surface deformation is smaller than other surface deformation processes, such as groundwater fluctuations or tectonic activity on other structures.

5.3. Structural Interpretation

The deformation pattern over the tableland corresponds well with the one expected from a pure-shear fault-bend fold above a back thrust with characteristic dimensions similar to the fold imaged on the seismic lines north of the tableland, strongly suggesting a similar deep structure beneath the whole area. The axis of the

fold is oriented N5°E in the southern part of the tableland and N40–45°E in the northern part, fairly similar to the fold orientation between Line D6 and Lines D1 and D5 and to the back thrust strike of N44°E inferred from D1 and D5. We interpret the back thrust inferred from the seismic lines as the northern continuity of the Houchiali fault, as the surface extrapolation of the back thrust is consistent in map view with the northward extrapolation of the ~N40°E fault scarp visible at the northern tip of the tableland. However, in map view, the fold axial surfaces are not strictly continuous from the northern part of the tableland to the seismic lines: Axial surfaces from the seismic lines are shifted ~2 km to the west, leading to a narrowing of the fold from ~8.5 km at the latitude of D5 to ~6.5 km at the center of the tableland (Figure 7a). We further discuss this discontinuity and the overall geometry of the fold and faults in the next section.

6. Discussion

6.1. Overall Geometry of the Houchiali Fault and Tainan Detachment and Relation to Regional Tectonic Structures

In this section we bring together the contributions from our study and from earlier works in order to propose and discuss a possible structural model for the Tainan anticline and surrounding faults that is compatible with all the available observations.

Seismic Lines D1 and D5, as well as D6 and rD1 (Figure 1a), located north of the Tainan Tableland, image a pure-shear fault-bend fold developing on an ~38°W dipping back thrust, interpreted as the continuation of the Houchiali fault, that roots on a 3.8-km-deep subhorizontal detachment within the Lower Gutingkeng mudstone. This detachment is referred to as the Tainan detachment (Le Béon et al., 2017). The fold appears to have vanished at the latitude of Seismic Line rD2 (Figure 1a). In contrast, southward, the topography of the tableland and the InSAR SR velocity pattern are also consistent with a pure-shear fault-bend fold of similar first-order geometry and dimensions as in the north. This suggests that the Tainan anticline formed above a similar wedge structure that extends from Lines D1, D5, and rD1 toward the south under the tableland. Yet the structural map in Figure 7a shows a discontinuity in the northern part of the fold between the axial surfaces mapped from InSAR SR velocity and those mapped from the seismic lines, meaning that the second-order structure of the fold is likely changing at this latitude, as discussed later in this section.

The seismic lines do not allow constraining the geometry of the back thrust and of the reflectors near the surface. In parallel, surface evidence for the Houchiali fault along the eastern edge of the Tainan Tableland is still lacking today (Lee, 2001a, 2001b, 2003; C. W. Lin et al., 2007), although the sharp deformation gradient observed from geodetic data during episodes interpreted as aseismic slip (Butcher and Huang, 2017; Fruneau et al., 2001; Huang et al., 2009, Huang, Bürgmann, et al., 2016, Huang, Hsin, et al., 2016) (Figure 7b) suggests a very shallow fault tip or a fault reaching the surface. Across the eastern edge of the tableland, shallow seismic reflection imaged east dipping reflectors down to ~600-m depth, capped by onlapping subhorizontal reflectors from ~100- to 120-m depth to the surface (Kuo, 1999), probably Holocene in age (Lu, 2006; Chen et al., 2004; Figure 6). Trenches and shallow boreholes at different latitudes across the scarp revealed east dipping Holocene strata with dips as steep as 35–55° (Lee, 2001a, 2001b, 2003; C. W. Lin et al., 2007). Therefore, similarly to trishear folds identified from trenches across the Chelungpu fault (M.-L. Lin et al., 2007; W.-J. Huang, Wen-Shan, et al., 2016), the Houchiali fault may progressively propagate upward and reach the near-surface as a fold forelimb that is probably partly buried under Holocene sediments (Figure 8).

The surface trace of the Houchiali fault, as extrapolated from Seismic Lines D1 and D5, is very close to the tip of the 1946 M6.3 earthquake surface rupture along the Hsinhua fault (Figures 1a and 7a). The Hsinhua fault is identified as a right-lateral, subvertical fault (Bonilla, 1975; C. W. Lin et al., 2007). It is inferred as a former Paleogene normal fault, reactivated as a tear fault during orogeny, as other approximately E-W strike-slip faults in western Taiwan (Brown et al., 2017; Pathier, 2003; Yang et al., 2016). The westward extent of the fault remains unknown. In their tectonic block model, Ching, Rau, et al. (2011) proposed an approximately N-S east dipping Tainan fault located west of Tainan Tableland, with the right-lateral Hsinhua fault extending westward until the Tainan fault. Instead, we propose a wedge delimited by the Tainan detachment and the Houchiali fault that abuts and slides westward against the reactivated right-lateral Hsinhua fault, which would terminate at the 1946 earthquake rupture tip. We do not exclude that the older Hsinhua normal fault could extend further westward, but it would be mainly inactive deeper than the detachment level. The
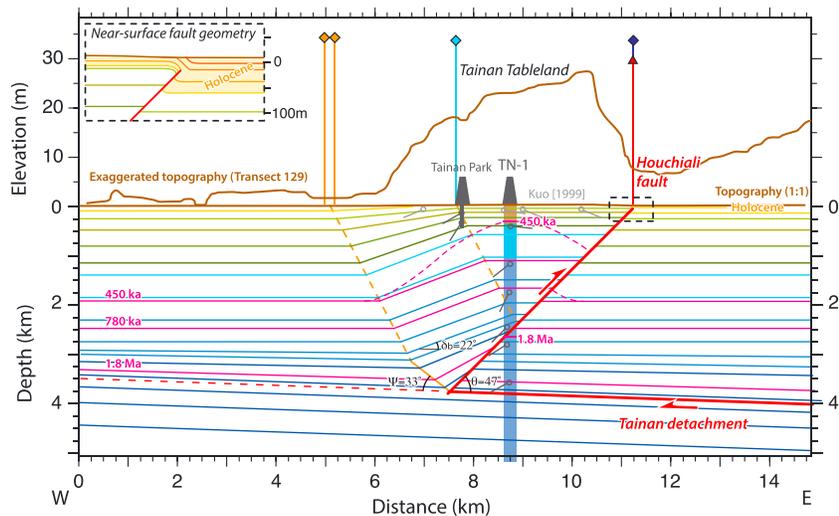
Figure 8. Schematic toy model of the pure-shear wedge fault-bend fold above the Houchiali back thrust at the latitude of the Tainan Tableland. See Figures 1 and 7 for the location of borehole TN-1 and topographic Transect 129. This model attempts to match the fold width as defined by axial surfaces inferred from topography and InSAR deformation pattern, following theoretical geometric relationships established for pure-shear fault-bend folds (Suppe et al., 2004). Age constraints come from nannostratigraphy and magnetostratigraphy (Chen et al., 2001; Chi, 1978; Covey, 1984a, 1984b; Horng, 1991; Yuan, 1987). Dated horizons indicated west of the tableland lie at similar depths as for the seismic lines D1 and D5. TN-1 borehole core dips are from Hsieh (1972) and could have any orientation. Some of the dip angles may be steeper because of downlapping structures or channels (see text). Nevertheless, the dip data and borehole nannostratigraphy, all together, suggest a higher relief for the fold than in our theoretical model.

structural models proposed by Ching, Rau, et al. (2011) and in this study would probably fit equally well GPS horizontal velocities based on an elastic block modeling approach. While we think that Ching et al.'s model served well the purpose of their study to estimate fault slip rates at the scale of the Taiwan mountain belt, we argue that their model does not satisfy the eastward vergence of the Tainan anticline.

Additional constraints on the regional subsurface structure are gained thanks to a series of seismic reflection profiles acquired north and east of the Tainan anticline (Figure 1a). We mentioned that the Tainan anticline has vanished at the latitude of Line rD2. Further north, all Seismic Lines rD3 to rD7 image another fold: a symmetric, long-wavelength anticline, which limbs are clearly defined by continuous reflectors and interpreted as a detachment fold, the Hsinying anticline. The fold mapping through the seismic lines defines an anticline axis oriented ~N20°E, roughly in the continuation of the Tainan anticline (Figure 1a). Although the quality of most seismic lines is poor deeper than 1.5-s two-way travel time, the transition between folded and undeformed reflectors is around ~2.0 s, which would correspond to ~3.0-km depth if we assume a similar velocity structure to the one of D1 and D5. The detachment lies at shallower depth compared to the Tainan anticline, yet the north-south seismic line rDNS shows a southward deepening of the basin, with both detachments corresponding to the same stratigraphic level. East of the Tainan Tableland, the low-quality Seismic Line T4 (Figure 1a) images a syncline axial surface with subhorizontal reflectors on the west part of the Dawan Lowland and west dipping reflectors on the eastern part. Deformed reflectors are clearly visible down to 2.0–2.2 s, while deeper reflectors seem subhorizontal, which suggests a detachment at ~2.3 s, similar to Seismic Lines D1 and D5. Therefore, the detachment appears to lie at a rather constant depth north of the tableland, a few kilometers eastward, and thus probably beneath the tableland as well. In addition, it uses the same layer over a broader region, extending northward at least to the Tsengwen River.

The discontinuity in the axial surfaces in Figure 7a consists in a narrowing of the fold by ~2 km toward the south. It is notably located at similar latitude to the Hsinhua fault. Theoretically, building a narrower fold requires a steeper back thrust, a shallower detachment, and/or a thinner basal shear layer (Figure 2c). While the Tainan Basin deepens southward at the regional scale, subsurface data demonstrated the existence within the northern Tainan Basin offshore Tainan of an Oligo-Miocene horst-and-graben structure, oriented

N60°E (Lin, 2001; Lin et al., 2003; Yang et al., 2006). The extension of this normal fault system on-land is unknown, as is its relationship with the inferred Hsinhua normal fault. Seismic Lines D1 and D5 show that the detachment lies near the base of the foreland basin sediments, which have irregular thickness as they on-lap postrifting passive margin sediments, and are also affected by channels. Regardless of the exact passive margin structure beneath the structural discontinuity, Lines D1 and D5 already point to variations in the stratigraphic architecture near the detachment level that could have affected the geometry and the development of the Tainan anticline. Because the detachment depth seems fairly constant from D1 and D5 to T4 (Figure 1a), we favor a steepening of the back thrust to explain the southward decrease in fold width. Considering a 3.8-km-deep detachment, a ~2-km reduction of the fold width would require a steepening of the back thrust from 38° to ~45°.

6.2. Tentative Estimate of the Cumulative Shortening at the Latitude of Tainan Tableland

Following the discussion above on the southward extrapolation of the pure-shear fault-bend fold model, this section attempts to build a schematic model of the fold at the latitude of the tableland. We compare the model with previous observations (Figure 8) and use it to estimate the cumulative shortening across the fold, with the goals to estimate the long-term shortening and to evaluate the significance of this frontal fold at the scale of the fold-and-thrust belt.

The detachment depth and the constraints on the fold width provided by the axial surface mapping based on InSAR and topography leave limited freedom on the fold geometry when fitted following the theoretical expectations for a pure-shear fault-bend fold (Suppe et al., 2004). We start with a fault dip of 45° and a dip of 2°E for the detachment (i.e., a wedge angle θ of 47°), a detachment depth of 3.8 km at the wedge tip, and a 560-m-thick basal shear layer, similar to D1 and D5. Then, the constraints on the fold axial surface locations lead to a back-limb dip δ_b of 22° and a dip angle ψ of 33° for the syncline axial surface within the basal pure-shear layer, close to the 36° predicted by the theoretical model. For these structural parameters, the theoretical relationships established for pure-shear fault-bend folds between fault dip, fold limb dip, shear layer thickness h, and total shortening S (Suppe et al., 2004) predict a shortening of 1.1 km, which corresponds to the structural relief component of shortening. This value is about twice the structural shortening determined north of the tableland (513 ± 43 m).

The schematic model, however, fails to fit the dips determined from the Tainan Park shallow borehole (C. W. Lin et al., 2007), from the borehole TN-1 (Hsieh, 1972), and from shallow seismic reflection in the southern part of the tableland (Kuo, 1999; Figure 8). The core dips from borehole TN-1 randomly vary from 28° to 64°, which makes them difficult to interpret and questions their representativeness. The presence of channels, for example, could lead to locally steeper dips than the surrounding bedding. Regarding Tainan Park borehole, a downlap sedimentary structure could also lead to steeper dips. Besides dip data, the estimated depths of the NN19–NN20 and NN18–NN19 nannozone transitions in borehole TN-1 (Covey, 1984b; Yuan, 1987) also suggest a higher relief for the fold than in our model. All together, these data probably indicate a more complex history of folding, in particular including a different folding mechanism at the fold initiation, as a detachment fold for example. Therefore, the 1.1-km structural shortening predicted from our schematic model is probably underestimated. At first order, layers with steeper dips and that would fit the nannozone depths in TN-1 (pink dashed line on Figure 8) indicate an area of relief that is up to twice the area of relief beneath our model layers, meaning a structural shortening in the order of 2.2 km or less. Hence, we bracket the cumulative structural shortening between 1.1 and 2.2 km.

To estimate the shortening consumed by horizontal compaction, we rely on the horizontal compaction shortening estimated along Seismic Line D6 (580 ± 100 m; section 3.2.2.) that we discuss in the light of fairly well-documented case examples from the frontal folds of the Nankai and Cascadia accretionary prisms (Bangs et al., 2004; Bangs and Gulick, 2005; Cochrane et al., 1994; Henry et al., 2003). The horizontal compaction shortening along D6 represents a minimum value for the latitude of the tableland, because shortening increases southward and because line D6 seismic velocity data set extends less than 3 km away from the fold. Horizontal compaction was estimated at 250–350 m in Nankai Trough, about four times the structural shortening, and at 300–600 m in Cascadia, about once to twice the structural shortening, with a similar horizontal stretch of ~0.9 in both cases (Gonzalez-Mieres and Suppe, 2006). Major differences between the two areas are the detachment depth and sediment porosity. The large contribution of horizontal compaction to shortening consumption in Nankai is likely facilitated by a very shallow detachment at ~700-m depth and a

high sediment porosity within the frontal fold (35–60%), while in Cascadia the detachment lies at ~2.5-km depth, with a lower sediment porosity within the frontal fold (10–28%), at least partly due to vertical compaction. In Tainan, the detachment lies at ~3.8-km depth, deeper than the Cascadia case, so that vertical compaction limits the sediment porosity. The porosity depth profile for D6 shows porosity values at 1.5-km depth (i.e., near the base of the growth strata) of 8% within the fold and 15% out of the fold, reaching 2–3% at 2.5-km depth out of the fold. Therefore, the potential for additional horizontal compaction across the central part of the fold compared to that along D6 appears to be limited to a few hundred meters at most. Thus, we propose a conservative range of 800 ± 200 m for the horizontal compaction shortening at the latitude of the tableland.

The structural shortening and horizontal compaction shortening estimates lead to a total shortening estimate in the order of 2–3 km. Even though this range is quite broad, it is a valuable piece of information when working on the restoration of a regional cross section and on the development of the fold-and-thrust belt. Because there is no constraint on when horizontal compaction began, we first use only the structural shortening of 1.1–2.2 km to calculate a minimum long-term shortening rate of 3–8 mm/a since 310 ± 50 ka at the latitude of the tableland. Now considering that the horizontal compaction shortening also occurred since 310 ± 50 ka, we obtain an upper bound for the shortening rate of 8–11 mm/a.

6.3. Rates of Uplift and Shortening at Different Timescales

The active present-day growth of the Tainan anticline is probably the best-monitored fold growth on Earth. Leveling, GPS, and InSAR measurements covering different time periods since 1996 (Ching, Hsieh, et al., 2011; Huang et al., 2009, Huang, Bürgmann, et al., 2016; Wu et al., 2013; CGS, 2014) converge to an average present-day uplift rate of 9–12 mm/a of the tableland relative to the Coastal Plain. Horizontal velocities based on continuous and campaign GPS measurements between 2002 and 2014 (CGS, 2014) progressively decrease from the toe of the foothills, in the east, to the coastline, in the west (Figure 1), clearly imaging the consumption of westward shortening. Yet geodetic data across shear fault-bend folds remain challenging to model for shortening rate determination, due to plastic deformation through thickening, limb rotation, and kink-band migration, as well as horizontal compaction. Such modeling is beyond the scope of this work. Based on island-scale block modeling of horizontal GPS velocities, Ching, Rau, et al. (2011) obtained a slip rate of 12 ± 5 mm/a on the so-called Tainan fault, an east dipping thrust located at the western edge of the Tainan tableland. Even though our study does not support the existence of such fault, we consider that Ching et al.'s approach still provides a meaningful estimate of the shortening rate consumed across the anticline.

The present-day uplift rate (9–12 mm/a) and shortening rate estimates (12 ± 5 mm/a; Ching, Rau, et al., 2011) are consistent with the uplift rate (8.7 ± 2.3 mm/a) and shortening rate (10.3 ± 1.0 mm/a) determined from Holocene strain markers. Hence, although rapid and transient, present-day deformation is representative of the longer-term Holocene cumulative deformation. The large uncertainty on the long-term shortening rate estimate (3–11 mm/a) limits further comparisons with the Holocene and present-day shortening rates. Shortening could either have occurred on a constant rate in the order of ~10 mm/a since the fold initiation, or it could have started at a slower rate as the detachment propagated westward, through horizontal compaction and the initial stage of folding, and later accelerated as the detachment became a mature dislocation plane. The structural shortening depth profile within the growth strata (Figure 3b) does not show any significant change in the shortening over sedimentation rate ratio (dS/dH) that could further document temporal variations in shortening rate, as reported by Gonzalez-Mieres and Suppe (2011) for other folds worldwide. This may support a scenario of constant shortening with time. Note that coincidental variations in shortening and sedimentation rates (e.g., a progressive increase with time) lead to a constant dS/dH ratio and therefore remain unnoticed in the shortening versus depth graph.

6.4. Implications for Regional Tectonics and Seismic Hazard Assessment
6.4.1. Regional Significance of the Tainan Anticline

The Tainan anticline is the frontal structure of the Western Foothills of the mountain belt, at a latitude where about 40 mm/a westward shortening is consumed (CGS, 2014; Tsai et al., 2015; Figure 1b). The Holocene shortening rate that we determined accounts for 25% of the regional shortening rate, making the anticline and the Houchiali fault a significant active structure at the scale of the fold-and-thrust belt. In contrast, the fold inception age of 310 ± 50 ka is very young, and the cumulative shortening of 2–3 km is limited in regard of the ~3-Ma deformation history of the foothills (Le Béon et al., 2017; Mouthereau et al., 2001).

At the regional scale, the Tainan detachment depth determined in this study is a key piece of information in order to build regional cross sections across the foothills of the mountain belt (Figure 1c). The Lower Gutingkeng Tainan detachment likely extends from the Tainan wedge tip to ~19 km to the east, beneath the Lungchuan triangle zone (Huang et al., 2004; Le Béon et al., 2017). In addition to the Houchiali fault, two other back thrusts root on this detachment, which accommodated limited cumulative shortening. Further east, the Tainan detachment must ramp down to a deeper detachment within the upper Miocene Changchihkeng formation (Huang et al., 2004; Le Béon et al., 2017). The east dipping Lungchuan fault and Pingchi fault ramp from this detachment, bringing upper Miocene formations to the surface. Although the faults in the hinterland accommodated a lot more shortening in the long term, the ramp and the frontal back thrusts appear to be the most active structures today (Pathier et al., 2014; Le Béon et al., 2017; Figure 1b). Two moderate magnitude earthquakes, the 2010 M_w6.3 Jia-Shian earthquake and the 2016 M_w6.4 Meinong earthquake, which epicenters were located ~50 and ~30 km east of Tainan Tableland, respectively (e.g. Ching, Johnson, et al., 2011; Huang et al., 2013, Huang, Hsin, et al., 2016), nucleated at deeper depths of 15–25 km than the structures drawn in Figure 1c cross section. Both events had oblique reverse faulting focal mechanisms that show that the middle crust is also involved in shortening. The geological structures that generated these events and their long-term contribution to shortening remain to be investigated. A M_w5.7 normal faulting event also occurred in 2017 ~15 km southwest of the Tainan Tableland and at ~15-km depth (www.cwb.gov.tw/V7e/earthquake). It is likely associated to the buried normal fault system identified offshore Tainan (e.g., Lin, 2001; Lin et al., 2003; Yang et al., 2006).

6.4.2. Aseismic Slip and Frictional Behavior

Numerous geodetic studies proposed the occurrence of aseismic slip on the Houchiali fault and Tainan detachment, as steady creep during periods of a few years or as transient events associated with or following local and regional earthquakes (Butcher and Huang, 2017; Ching, Rau, et al., 2011; Fruneau et al., 2001; Huang et al., 2006, 2009, Huang, Bürgmann, et al., 2016, Huang, Hsin, et al., 2016; Wu et al., 2013). Transient events, in particular, were observed not only on the tableland and across the Houchiali fault but also across some of the hinterland back thrusts (Figure 1c). They occurred coincidentally and/or a year after the 1999 Chi-Chi earthquake (M_w7.6, ~100 km away from Tainan), the 2016 Meinong earthquake (M_w6.4, ~30 km away), and probably the 2010 Jia-Shian earthquake (M_w6.3, ~50 km away from Tainan; Butcher and Huang, 2017; Huang et al., 2006, 2009, 2013, Huang, Hsin, et al., 2016; Le Béon et al., 2017). Focusing on the Tainan anticline, the deformation associated with the 2016 Meinong earthquake was well monitored during and after the event, using Sentinel-1A images. Coseismic line-of-sight displacements in the order of 1.5–2.0 cm were monitored on Tainan Tableland, and line-of-sight displacements of a similar to twice larger amplitude were observed during more than a year after the earthquake (Butcher and Huang, 2017; Huang, Hsin, et al., 2016). All together, these studies suggest that aseismic slip may release a nonnegligible part of tectonic stress.

Aseismic behavior requires a very low effective friction on the detachment and back thrusts that likely arises from the combination of a weak lithology, an elevated pore-fluid pressure and a low normal stress related to relatively shallow depths. The frictional behavior of the fault may be described as velocity strengthening (Scholz, 1998). In eastern Taiwan, the creeping behavior of the Longitudinal Valley Fault was associated to the Lichi mélange, composed of highly comminuted grains, abundant clay, and nannofossils providing calcite enhancing pressure dissolution (Thomas et al., 2014). The Lower Gutingkeng formation shares similar properties, as it consists mainly of clay-rich mudstone with intercalated fine-grained sandstone beds and contains nannofossils (e.g., Chi, 1978, 1979; Horng and Shea, 1994). In addition, high pore-fluid pressure was observed in the TN1 borehole a few hundred meters above the detachment (Huang et al., 2004). Besides aseismic slip, the low friction related to the Gutingkeng mudstone, combined with a high sedimentation rate during deformation, that is, during the Middle to Late Pleistocene (1.8–4.5 mm/a; Chang & Chi, 1983; Chen et al., 2001; Teng, 1990; this study), may also explain the development of landward verging structures at the mountain front (Figure 1c), with aseismic behavior enabled by the elevated pore-fluid pressure (Cubas et al., 2016).

6.4.3. Seismic Hazard Assessment of the Houchiali Fault

This study provides new evidence and clues for active faults geometry, as well as a fairly well constrained Holocene shortening rate, consistent with previously published present-day fault slip rate based on geodetic data (Ching, Rau, et al., 2011). These are key parameters for defining earthquake source topologies and

earthquake recurrence intervals used to assess probabilistic seismic hazard in Taiwan (Lee et al., 2017; Shyu et al., 2016; Wang et al., 2016). Because of rapid shortening rates and of the seismic wave propagation properties within the sedimentary basin, the hazard probability in Tainan area was found to be among the highest across the Taiwan Island. However, these predictions, which were the firsts of the kind in Taiwan, did not consider stress release through aseismic slip in the Tainan area. Besides aseismic slip, horizontal compaction, which accounts for at least 24%, and possibly 30–50%, of E-W shortening in the long term, also is a mechanism of shortening consumption that lowers the amount of slip to be released on faults during earthquakes. In the following, we discuss the effect of aseismic slip and frictional behavior on the evaluation of seismic hazard related to the Houchiali fault.

Based on the fault length ($L = 15$ km) and downdip width (5 to 6 km) estimated from the detachment depth and a fault dip of 45°, we use the earthquake fault scaling relationships of Leonard (2010) to assess the moment magnitude and average displacement associated with an earthquake on the Houchiali fault. For a width of 5–6 km, Leonard (2010) scaling points to a rupture length of 5–7 km, yet the database suggests that a rupture of the entire fault remains possible. The rupture of a 6-km-long section of the Houchiali fault would generate a M_w5.7-5.8 earthquake with 20-cm average displacement D, and the rupture of the entire fault would generate a M_w5.9–6.2 earthquake with $D = 45$ cm. Although moderate, such an event that nucleates at shallow depth beneath a 1-million-inhabitants city could cause significant casualties and damage, related to ground shaking and liquefaction, as experienced during the 2016 M_w6.4 Meinong earthquake (CGS, 2016), which hypocenter was located 30 km east of Tainan and 15 km deep.

Next, we need to estimate the recurrence interval of such events. We consider a fault slip rate of 11.8 $\pm$ 1.2 mm/a, based on the Holocene shortening rate (10.3 $\pm$ 1.0 mm/a) and Suppe et al. (2004) kinematic model for pure-shear fault-bend folds ($\theta = 47°$; $\delta_b = 22°$). Since we do not know the proportion of shortening that is released aseismically, we first assume a fully locked fault. Then, the moderate magnitude events suggested by Leonard (2010) scaling laws would occur every 15 to 40 years. Historical earthquake records in Tainan area clearly do not match this hypothesis. The records attest for four destructive earthquakes (M_w~6–7) in the region between 1655 and 1721 and little activity afterward (Ng et al., 2009), until the M_w6.3 earthquake that ruptured the Hsinhua fault in 1946 (Bonilla, 1975). Historical accounts do not allow determining the fault responsible for these events, yet they imply that the Houchiali fault did not produce a significant earthquake since at least 300 years. Considering that the most recent event occurred at least 300 years ago and was a M_w5.7–6.2 earthquake with 20- to 45-cm average slip, we deduce a maximum fault slip rate of 0.7–1.5 mm/a. This value corresponds to the effective loading rate on the fault, defined as fault slip rate minus aseismic slip rate and rate of horizontal compaction. The large discrepancy between the 300-year loading rate and the present-day and Holocene shortening rates implies that shortening during the last 300 years was largely consumed through frequent aseismic slip events, plus a possible contribution of horizontal compaction.

Therefore, accounting for aseismic slip would considerably lower the seismic hazard related to the Houchiali fault, with the difficulty to also consider that the fault behavior might evolve to stick slip at timescales longer than a few decades or several centuries. Hence, it is important to keep monitoring crustal deformation in the area. While velocity strengthening inhibits earthquake nucleation on the fault (Scholz, 1998), friction experiments on clay-rich sediments indicated favorable rupture propagation within clay-rich fault zones (Faulkner et al., 2011). This means that creeping fault segments could be involved in large-magnitude events, as it was suggested to have happened during the 2011 Tohoku-Oki event of Japan, in a subduction context (Noda & Lapusta, 2013).

7. Conclusions

Based on a multidisciplinary approach, we constrained the geometry, the mechanisms of shortening, and the deformation history of the Tainan Anticline, a frontal fold of the foothills of southwestern Taiwan. We identified the anticline as a pure-shear fault-bend-fold growing on a west dipping back thrust, the Houchiali fault, that roots on a subhorizontal shallow detachment at ~3.8-km depth, within the Lower Gutingkeng mudstone, which appears to act as a regional detachment level. The central part of the fold may have had a more complex growth history at the origin of higher relief than that of the theoretical model. The fold started growing 310 $\pm$ 50 ka ago. We determined a total shortening of 673 $\pm$ 83 m near the northern tip of

the fold, including a contribution of 24% of horizontal compaction. In the central part of the fold, we estimated the total shortening to 2–3 km, with ~30–50% of horizontal compaction. Horizontal compaction, and hence total shortening, may have been underestimated as we used proxies for porosity within only a few kilometers away from the fold. Additional data offshore may help better evaluate the significance of horizontal compaction in the future. The long-term Late-Pleistocene (310 ka) shortening rate is estimated to 3–11 mm/a. The Holocene shortening rate of 10.3 ± 1.0 mm/a that we determined is compatible with a previously published present-day fault slip rate of 12 ± 5 mm/a based on geodesy and shows that the Tainan anticline consumes 25% of the shortening consumed across the foothills of southwestern Taiwan. The relatively fast Holocene shortening rate and the very shallow depth of the Houchiali fault and Tainan detachment pose a threat to Tainan city, although the relatively small area of the fault would limit the earthquake magnitude to ≤6. The lack of seismicity during the last three centuries (Ng et al., 2009) shows that stress release through aseismic slip, as observed from geodesy during the past two decades (Butcher and Huang, 2017; Huang et al., 2006, 2009, Huang, Bürgmann, et al., 2016; Wu et al., 2013; CGS, 2014), is probably a representative mechanism of the longer-term slip behavior of the fault and detachment. The question remains whether these aseismic slip periods partially or totally release stress. Hence, it is important to carry on with constant monitoring of ground-surface deformation in the area using geodetic techniques, as it was done in the past.

The Tainan Anticline shares similarities with other frontal folds worldwide. It is a pure-shear fault-bend fold, which along with pure-shear detachment folds is a common feature at the toes of mountain belts or accretionary prisms, as described in section 1. Horizontal compaction also appears as a significant mechanism to accommodate shortening. This was previously observed in Nankai and Cascadia (Gonzalez-Mieres and Suppe, 2011), yet it remains poorly documented worldwide. Peculiar features of the Tainan anticline include the back thrust wedge structure, which seems to repeat in the foothills further inland (Le Béon et al., 2017; Figure 1c) and the aseismic slip behavior. Aseismic slip is certainly favored by low friction within the high-pore pressure Gutingkeng mudstone, which hosts the Tainan detachment and the Houchiali fault. By analogy with mechanical models of accretionary prism (Cubas et al., 2016), the low friction, combined with a high syntectonic sedimentation rate, may also explain the development of landward verging structures at the mountain front. The stratigraphic architecture of the passive margin and foreland basin may also have played a role in the fold development.

References

Argus, D. F., Gordon, R. G., & DeMets, C. (2011). Geologically current motion of 56 plates relative to the no-net-rotation reference frame. *Geochemistry, Geophysics, Geosystems*, *12*, Q11001. https://doi.org/10.1029/2011GC003751

Bangs, N. L., Shipley, T. H., Gulick, S. P. S., Moore, G. F., Kuromoto, S., & Nakamura, Y. (2004). Evolution of the Nankai Trough décollement from the trench into the seismogenic zone: Inferences from three-dimensional seismic reflection imaging. *Geology*, *32*(4), 273–276. https://doi.org/10.1130/G20211.2

Bangs, N. L. B., & Gulick, S. P. S. (2005). Physical properties along the developing decollement in the Nankai Trough: Inferences from 3-D seismic reflection data inversion and Leg 190 and 196 drilling data. In H. Mikada, G. F. Morre, A. Taira, K. Becker, J. C. Moore, & A. Laus (Eds.) *Proceedings of Ocean Drilling Program Legs 190/196, Scientific Results* (Chap. 12, pp. 1–18).

Bard, E., Hamelin, B., Arnold, M., Montaggioni, L., Cabioch, G., Faure, G., & Rougerie, F. (1996). Deglacial sea-level record from Tahiti corals and the timing of global meltwater discharge. *Nature*, *382*(6588), 241–244. https://doi.org/10.1038/382241a0

Biete, C., Alvarez-Marron, J., Brown, D., & Kuo-Chen, H. (2018). The structure of southwest Taiwan: The development of a fold-and-thrust belt on a margins outer shelf and slope. *Tectonics*, *37*, 1973–1993. https://doi.org/10.1029/2017TC004910

Bonilla, M.G., (1975). A review of recently active faults in Taiwan (Report No. 75–41), Open-File Report. Reston, VA.

Brown, D., Alvarez-Marron, J., Biete, C., Kuo-Chen, H., Camanni, G., & Ho, C.-W. (2017). How the structural architecture of the Eurasian continental margin affects the structure, seismicity, and topography of the south central Taiwan fold-and-thrust belt. *Tectonics*, *36*, 1275–1294. https://doi.org/10.1002/2017TC004475

Butcher, R., & Huang, M.-H., (2017). Using InSAR time series analysis to interpret co- and postseismic deformation of the 2016 Mw 6.4 MeiNong earthquake in SW Taiwan. Presented at the AGU Fall Meeting, New Orleans, LA.

Central Geological Survey, (2014). Report on geodetic monitoring of active faults 2/4. Ministry of Economic Affairs, Taiwan, R.O.C.

Central Geological Survey, (2016). Report on the 2016/02/06 earthquake. Ministry of Economic Affairs, Taiwan, R.O.C.

Chang, S. S. L., & Chi, W.-R. (1983). Neogene nannoplankton biostratigraphy in Taiwan and the tectonic implications. *Petroleum Geology of Taiwan*, *19*, 93–147.

Chappell, J., & Polach, H. (1991). Post-glacial sea-level rise from a coral record at Huon Peninsula, Papua New Guinea. *Nature*, *349*(6305), 147–149. https://doi.org/10.1038/349147a0

Chen, W.-S., Ridgway, K. D., Horng, C.-S., Chen, Y.-G., Shea, K.-S., & Yeh, M.-G. (2001). Stratigraphic architecture, magnetostratigraphy, and incised-valley systems of the Pliocene-Pleistocene collisional marine foreland basin of Taiwan. *GSA Bulletin*, *113*(10), 1249–1271. https://doi.org/10.1130/0016-7606(2001)113<1249:SAMAIV>2.0.CO;2

Chen, W.-S., Sung, S.-H., Wu, L.-C., Hsu, H.-D., & Yang, H.-C. (2004). Shoreline changes in the coastal plain of Taiwan since last glacial epoch. *Bulletin Department of Anthropology*, *62*, 40–55. (in Chinese)

Chen, Y.-G., & Liu, T.-K. (2000). Holocene uplift and subsidence along an active tectonic margin southwestern Taiwan. *Quaternary Science Reviews*, *19*(9), 923–930. https://doi.org/10.1016/S0277-3791(99)00076-1

Chi, W.-R. (1978). The late Neogene nannobiostratigraphy in the Tainan foothills region, southern Taiwan. *Petroleum Geology of Taiwan*, *15*, 89–125.

Chi, W.-R. (1979). A biostratigraphic study of the Late Neogene sediments in the Kaohsiung area based on calcareous nannofossils. *Proceedings of the Geological Society of China*, *22*, 121–144.

Ching, K.-E., Hsieh, M.-L., Johnson, K. M., Chen, K.-H., Rau, R.-J., & Yang, M. (2011). Modern vertical deformation rates and mountain building in Taiwan from precise leveling and continuous GPS observations, 2000–2008. *Journal of Geophysical Research*, *116*, B08406. https://doi.org/10.1029/2011JB008242

Ching, K.-E., Johnson, K. M., Rau, R.-J., Chuang, R. Y., Kuo, L.-C., & Leu, P.-L. (2011). Inferred fault geometry and slip distribution of the 2010 Jiashian, Taiwan, earthquake is consistent with a thick-skinned deformation model. *Earth and Planetary Science Letters*, *301*(1-2), 78–86. https://doi.org/10.1016/j.epsl.2010.10.021

Ching, K.-E., Rau, R.-J., Johnson, K. M., Lee, J.-C., & Hu, J.-C. (2011). Present-day kinematics of active mountain building in Taiwan from GPS observations during 1995–2005. *Journal of Geophysical Research*, *116*, B09405. https://doi.org/10.1029/2010JB008058

Cochrane, G. R., Moore, J. C., MacKay, M. E., & Moore, G. F. (1994). Velocity and inferred porosity model of the Oregon accretionary prism from multichannel seismic reflection data: Implications on sediment dewatering and overpressure. *Journal of Geophysical Research*, *99*(B4), 7033–7043. https://doi.org/10.1029/93JB03206

Corredor, F., Shaw, J., & Bilotti, F. (2005). Structural styles in the deep-water fold and thrust belts of the Niger Delta. *AAPG Bulletin*, *89*(6), 753–780. https://doi.org/10.1306/02170504074

Covey, M. (1984a). Lithofacies analysis and basin reconstruction, Plio-Pleistocene western Taiwan foredeep. *Petroleum Geology of Taiwan*, *20*, 53–83.

Covey, M., (1984b). Sedimentary and tectonic evolution of the western Taiwan foredeep (Ph.D Thesis). Princeton University.

Covey, M. (1986). The evolution of foreland basins to steady state: Evidence from the western Taiwan foreland basin. In P. A. Allen, & P. Homewood (Eds.), *Foreland Basins*, *Spec. Publs. int. Ass. Sediment.*, (Vol. 8, pp. 77–90). Oxford: Blackwell.

Cubas, N., Souloumiac, P., & Singh, S. C. (2016). Relationship link between landward vergence in accretionary prisms and tsunami generation. *Geology*, *44*(10), 787–790. https://doi.org/10.1130/G38019.1

Dumouchel, W., & O'Brien, F. (1991). *Computing and graphics in statistics* (pp. 41–48). New York, NY, USA: Springer-Verlag New York, Inc.

Eichelberger, N. W., Nunns, A. G., Groshong, R. H. J., & Hughes, A. N. (2017). Direct estimation of fault trajectory from structural relief. *AAPG Bulletin*, *101*(05), 635–653. https://doi.org/10.1306/08231616065

Epard, J.-L., & Groshong, R. H. (1993). Excess area and depth to detachment. *AAPG Bulletin*, *77*, 1291–1302.

Epard, J.-L., & Groshong, R. H. (1995). Kinematic model of detachment folding including limb rotation, fixed hinges and layer-parallel strain. *Tectonophysics*, *247*(1-4), 85–103. https://doi.org/10.1016/0040-1951(94)00266-C

Fairbanks, R. G. (1989). A 17,000-year glacio-eustatic sea level record: Influence of glacial melting rates on the Younger Dryas event and deep-ocean circulation. *Nature*, *342*(6250), 637–642. https://doi.org/10.1038/342637a0

Faulkner, D. R., Mitchell, T. M., Behnsen, J., Hirose, T., & Shimamoto, T. (2011). Stuck in the mud? Earthquake nucleation and propagation through accretionary forearcs. *Geophysical Research Letters*, *38*, L18303. https://doi.org/10.1029/2011GL048552

Fruneau, B., Pathier, E., Raymond, D., Deffontaines, B., Lee, C.-T., Wang, H. T., et al. (2001). Uplift of Tainan Tableland (SW Taiwan) revealed by SAR Interferometry. *Geophysical Research Letters*, *28*(16), 3071–3074. https://doi.org/10.1029/2000GL012437

Gonzalez-Mieres, R., & Suppe, J. (2006). Relief and shortening in detachment folds. *Journal of Structural Geology*, *28*(10), 1785–1807. https://doi.org/10.1016/j.jsg.2006.07.001

Gonzalez-Mieres, R., & Suppe, J. (2011). Shortening histories in active detachment folds based on area-of-relief methods. *AAPG Memoir*, *94*, 39–67. https://doi.org/10.1306/13251332M943428

Grando, G., & McClay, K. (2007). Morphotectonics domains and structural styles in the Makran accretionary prism, offshore Iran. *Sedimentary Geology*, *196*(1-4), 157–179. https://doi.org/10.1016/j.sedgeo.2006.05.030

Groshong, R. H. (2015). Quality control and risk assessment of seismic profiles using area-depth-strain analysis. *Interpretation*, *3*(4), SAA1–SAA15. https://doi.org/10.1190/INT-2015-0010.1

Hamilton, E. L. (1978). Sound velocity-density relations in sea-floor sediments and rocks. *The Journal of the Acoustical Society of America*, *63*(2), 366–377. https://doi.org/10.1121/1.381747

Hardy, S., & Connors, C. D. (2006). Short note: A velocity description of shear fault-bend folding. *Journal of Structural Geology*, *28*(3), 536–543. https://doi.org/10.1016/j.jsg.2005.12.015

Henry, P., Jouniaux, L., Screaton, E. J., Hunze, S., & Saffer, D. M. (2003). Anisotropy of electrical conductivity record of initial strain at the toe of the Nankai accretionary wedge. *Journal of Geophysical Research*, *108*(B9), 2407. https://doi.org/10.1029/2002JB002287

Ho, C. S. (1986). A synthesis of the geologic evolution of Taiwan. *Tectonophysics*, *125*(1-3), 1–16. https://doi.org/10.1016/0040-1951(86)90004-1

Holland, P. W., & Welsch, R. E. (1977). Robust regression using iteratively reweighted least-squares. *Communications in Statistics - Theory and Methods*, *6*, (9), 813–827. https://doi.org/10.1080/03610927708827533

Horng, C.-S., (1991). Study of magnetic minerals and magnetostratigraphy of the Tsengwenchi and Erhjenchi sections, southwestern Taiwan (Ph.D Thesis). National Taiwan University, Taipei.

Horng, C.-S., & Shea, K.-S. (1994). Study of nannofossil biostratigraphy in the eastern part of the Erhjen-Chi section, southwestern Taiwan. *Special Publication of the Central Geological Survey*, *8*, 181–204.

Hsieh, S. H. (1972). Subsurface geology and gravity anomalies of the Tainan and Chungchou structures of the Coastal Plain of southwestern Taiwan. *Petroleum Geology of Taiwan*, *10*, 323–338.

Hsu, Y.-J., Yu, S.-B., Simons, M., Kuo, L.-C., & Chen, H.-Y. (2009). Interseismic crustal deformation in the Taiwan plate boundary zone revealed by GPS observations, seismicity, and earthquake focal mechanisms. *Tectonophysics*, *479*(1-2), 4–18. https://doi.org/10.1016/j.tecto.2008.11.016

Huang, M.-H., Bürgmann, R., & Hu, J.-C. (2016). Fifteen years of surface deformation in Western Taiwan: Insight from SAR interferometry. *Tectonophysics*, *692*, 252–264. https://doi.org/10.1016/j.tecto.2016.02.021

Huang, M.-H., Dreger, D., Bürgmann, R., Yoo, S.-H., & Hashimoto, M. (2013). Joint inversion of seismic and geodetic data for the source of the 2010 March 4, Mw 6.3 Jia-Shian, SW Taiwan, earthquake. *Geophysical Journal International*, *193*(3), 1608–1626. https://doi.org/10.1093/gji/ggt058

Huang, M.-H., Hsin, T., Fielding, E. J., Hsin-Hua, H., Liang, C., Chung, H., & Hu, J.-C. (2016). Multiple fault slip triggered above the 2016 Mw 6.4 MeiNong earthquake in Taiwan. *Geophysical Research Letters*, *43*, 7459–7467. https://doi.org/10.1002/2016GL069351

Huang, M.-H., Hu, J.-C., Ching, K.-E., Rau, R.-J., Hsieh, C.-S., Pathier, E., et al. (2009). Active deformation of Tainan tableland of southwestern Taiwan based on geodetic measurements and SAR interferometry. *Tectonophysics*, *466*(3-4), 322–334. https://doi.org/10.1016/j.tecto.2007.11.020

Huang, M.-H., Hu, J.-C., Chia-Sheng, H., Kuo-En, C., Ruey-Juin, R., Erwan, P., et al. (2006). A growing structure near the deformation front in SW Taiwan as deduced from SAR interferometry and geodetic observation. *Geophysical Research Letters*, *33*, L12305. https://doi.org/10.1029/2005GL025613

Huang, S.-T., Yang, K.-M., Hung, J.-H., Wu, J.-C., Ting, H.-H., Mei, W.-W., et al. (2004). Deformation front development at the northeast margin of the Tainan Basin, Tainan–Kaohsiung area, Taiwan. *Marine Geophysical Researches*, *25*(1-2), 139–156. https://doi.org/10.1007/s11001-005-0739-z

Huang, W.-J., Wen-Shan, C., Lee, Y.-H., Yang, C.-C., Lin, M.-L., Cheng-Shing, C., et al. (2016). Insights from heterogeneous structures of the 1999 Mw 7.6 Chi-Chi earthquake thrust termination in and near Chushan excavation site, Central Taiwan. *Journal of Geophysical Research: Solid Earth*, *121*, 339–364. https://doi.org/10.1002/2015JB012174

Hubert-Ferrari, A., Suppe, J., Gonzalez-Mieres, R., & Wang, X. (2007). Mechanisms of active folding of the landscape (southern Tian Shan, China). *Journal of Geophysical Research*, *112*, B03S09. https://doi.org/10.1029/2006JB004362

Hubert-Ferrari, A., Suppe, J., Wang, X., & Jia, C. (2005). Yakeng detachment fold, South Tianshan, China. In *AAPG Seismic Atlas: Seismic Interpretation of Contractional Fault-Related Folds*, (pp. 110–113). Tulsa, Oklahoma, U.S.A: AAPG Studies in Geology.

Ingram, G., Chisholm, T., Grant, C., Hedlund, C., Stuart-Smith, P., & Teasdale, J. (2004). Deepwater North West Borneo: Hydrocarbon accumulation in an active fold and thrust belt. *Marine and Petroleum Geology*, *21*(7), 879–887. https://doi.org/10.1016/j.marpetgeo.2003.12.007

Kuo, H.-Y., (1999). Detecting Houchiali Fault and its neighboring structures using shallow seismic reflection method (Masther Thesis). National Central University.

Lacombe, O., Mouthereau, F., Deffontaines, B., Angelier, J., Chu, H. T., & Lee, C. T. (1999). Geometry and Quaternary kinematics of fold-and-thrust units of southwestern Taiwan. *Tectonics*, *18*(6), 1198–1223. https://doi.org/10.1029/1999TC900036

Laubscher, H. P. (1961). Die Fernschubhypothese der Jurafaltung. *Eclogae Geologicae Helvetiae*, *54*, 221–282.

Le Béon, M., Huang, M.-H., Suppe, J., Huang, S.-T., Pathier, E., Huang, W.-J., et al. (2017). Shallow geological structures triggered during the Mw 6.4 Meinong earthquake, southwestern Taiwan. *Terrestrial, Atmospheric and Oceanic Sciences*, *10*. https://doi.org/10.3319/TAO.2017.03.20.02

Lee, C.-T., (2001a). Analysis of drilling data across the Houchiali fault, using HQ continuous sampling technique (Report). Institute of Applied Geology, National Central University.

Lee, C.-T., (2001b). Paleoseismologic trenches across the Houchiali fault (Report). Institute of Applied Geology, National Central University.

Lee, C.-T., (2003). Paleoseismologic trenches across the Houchiali fault (Report). Institute of Applied Geology, National Central University.

Lee, Y.-H., Byrne, T., Wang, W.-H., Lo, W., Rau, R.-J., & Lu, H.-Y. (2015). Simultaneous mountain building in the Taiwan orogenic belt. *Geology*, *43*(5), 451–454. https://doi.org/10.1130/G36373.1

Lee, Y.-T., Wang, Y.-J., Chan, C.-H., & Ma, K.-F. (2017). The 2016 Meinong earthquake to TEM PSHA2015. *Terrestrial, Atmospheric and Oceanic Sciences*, *28*(5), 703–713. https://doi.org/10.3319/TAO.2016.12.28.02

Leonard, M. (2010). Earthquake fault scaling: Self-consistent relating of rupture length, width, average displacement, and moment release. *Bulletin of the Seismological Society of America*, *100*(5A), 1971–1988. https://doi.org/10.1785/0120090189

Liao, W.-Z., Lin, A. T., Liu, C.-S., Oung, J.-N., & Wang, Y. (2016). A study on tectonic and sedimentary development in the rifted northern continental margin of the South China Sea near Taiwan. *Interpretation*, *4*(3), SP47–SP65. https://doi.org/10.1190/INT-2015-0209.1

Lieske, J. (2000). Low-cost approach to depth correction of printed seismic sections. *Offshore Magazine February*, *2000*, 117–118.

Lin, A. T. (2001). *Cenozoic stratigraphy and tectonic development of the West Taiwan basins*. Oxford, UK: University of Oxford.

Lin, A. T., Liu, C.-S., Lin, C.-C., Schnurle, P., Chen, G.-Y., Liao, W.-Z., et al. (2008). Tectonic features associated with the overriding of an accretionary wedge on top of a rifted continental margin: An example from Taiwan. *Marine Geology*, *255*(3-4), 186–203. https://doi.org/10.1016/j.margeo.2008.10.002

Lin, A. T., Watts, A. B., & Hesselbo, S. P. (2003). Cenozoic stratigraphy and subsidence history of the South China Sea margin in the Taiwan region. *Basin Research*, *15*(4), 453–478. https://doi.org/10.1046/j.1365-2117.2003.00215.x

Lin, C. C. (1969). Holocene geology of Taiwan. *Acta Geologica Taiwanica*, *13*, 83–126.

Lin, C.-W., Lu, S.-D., Shi, T.-S., Chang, H.-C., & Shi, R.-C. (2000). *Field investigation on four suspected active faults in southwestern Taiwan*, *Spec. Publ. Centr. Geol. Surv.*, (Vol. 13, pp. 77–101).

Lin, C.-W., Lu, S.-T., Shih, T.-S., Lin, W.-H., Liu, Y.-C., & Chen, P.-T. (2007). *Active faults in southwestern Taiwan*, *Spec. Publ. Centr. Geol. Surv.*, (Vol. 17, p. 141).

Lin, K.-C., Hu, J.-C., Ching, K.-E., Angelier, J., Rau, R.-J., Yu, S.-B., et al. (2010). GPS crustal deformation, strain rate, and seismic activity after the 1999 Chi-Chi earthquake in Taiwan. *Journal of Geophysical Research*, *115*, B07404. https://doi.org/10.1029/2009JB006417

Lin, M.-L., Wang, C. P., Chen, W. S., Yang, C. N., & Jeng, F. S. (2007). Inference of trishear-faulting processes from deformed pregrowth and growth strata. *Journal of Structural Geology*, *29*(7), 1267–1280. https://doi.org/10.1016/j.jsg.2007.03.017

Lisiecki, L. E., & Raymo, M. E. (2005). A Pliocene-Pleistocene stack of 57 globally distributed benthic δ18O records. *Paleoceanography*, *20*, PA1003. https://doi.org/10.1029/2004PA001071

Lu, C.-C., (2006). Stratigraphy and Tectonics of the Southwestern Plain of Taiwan Since the Last Glacial Epoch (Masther Thesis). National Central University, Taoyuan.

McClay, K. (2011). Introduction to thrust fault-related folding. In K. McClay, J. Shaw, & J. Suppe (Eds.), *Thrust Fault-Related Folding*, *AAPG Memoir 94*, (pp. 1–19).

Mouthereau, F., Lacombe, O., Deffontaines, B., Angelier, J., & Brusset, S. (2001). Deformation history of the southwestern Taiwan foreland thrust belt: Insights from tectono-sedimentary analyses and balanced cross-sections. *Tectonophysics*, *333*(1-2), 293–322. https://doi.org/10.1016/S0040-1951(00)00280-8

Ng, S. M., Angelier, J., & Chang, C.-P. (2009). Earthquake cycle in Western Taiwan: Insights from historical seismicity. *Geophysical Journal International*, *178*(2), 753–774. https://doi.org/10.1111/j.1365-246X.2009.04164.x

Noda, H., & Lapusta, N. (2013). Stable creeping fault segments can become destructive as a result of dynamic weakening. *Nature*, *493*(7433), 518–521. https://doi.org/10.1038/nature11703

Pan, Y. S. (1968). Interpretation and seismic coordination of the Bouguer gravity anomalies obtained in southwestern Taiwan. *Petroleum Geology of Taiwan*, *6*, 197–208.

Pathier, E., (2003). Apports de l'interférométrie radar différentielle à la tectonique active de Taiwan (Ph.D Thesis). Université de Marne-la-Vallée.

Pathier, E., Fruneau, B., Doin, M.-P., Liao, Y.-T., Hu, J.-C., Champenois, J., (2014). What are the tectonic structures accommodating the present-day tectonic deformation in South-Western Taiwan? A new interpretation from ALOS-1 InSAR and GPS interseismic measurements. Presented at the Geodynamics and Environment in East-Asia. 7th France-Taiwan Earth Sciences Symposium, Hualien, Taiwan.

Schlische, R. W., Groshong, R. H., Withjack, M. O., & Hidayah, T. N. (2014). Quantifying the geometry, displacements, and subresolution deformation in thrust-ramp anticlines with growth and erosion: From models to seismic-reflection profile. *Journal of Structural Geology*, *69*, 304–319. https://doi.org/10.1016/j.jsg.2014.07.012

Scholz, C. H. (1998). Earthquakes and friction laws. *Nature*, *391*(6662), 37–42. https://doi.org/10.1038/34097

Shaw, J. H., Connors, C. D., & Suppe, J. (2005). *AAPG seismic atlas: Seismic interpretation of contractional fault-related folds*, *AAPG studies in geology*, (). Tulsa, Oklahoma, U.S.A: AAPG Studies in Geology.

Shyu, J. B. H., Chuang, Y.-R., Chen, Y.-L., Lee, Y.-R., & Cheng, C.-T. (2016). A new on-land seismogenic structure source database from the Taiwan Earthquake Model (TEM) project for seismic hazard analysis of Taiwan. *Terrestrial, Atmospheric and Oceanic Sciences*, *27*(3), 311–323. https://doi.org/10.3319/TAO.2015.11.27.02(TEM)

Sun, S. C. (1964). Photogeologic study of the Tainan-Kaohsiung Coastal Plain area, Taiwan. *Petroleum Geology of Taiwan*, *3*, 39–51.

Suppe, J. (1983). Geometry and kinematics of fault-bend folding. *American Journal of Science*, *283*(7), 684–721. https://doi.org/10.2475/ajs.283.7.684

Suppe, J. (1984). Kinematics of arc-continent collision, flipping of subduction, and back-arc spreading near Taiwan. *Memoir of Geological Society of China*, *6*, 21–33.

Suppe, J. (2011). Mass balance and thrusting in detachment folds. *AAPG Memoir*, *94*, 21–37.

Suppe, J. (2014). Fluid overpressures and strength of the sedimentary upper crust. *Journal of Structural Geology*, *69*, 481–492. https://doi.org/10.1016/j.jsg.2014.07.009

Suppe, J., Chou, G. T., & Hook, S. P. (1992). Rates of folding and faulting determined from growth strata. In K. R. McClay (Ed.), *Thrust Tectonics*, (pp. 105–121). London: Chapman & Hall.

Suppe, J., Connors, C. D., & Zhang, Y. (2004). Shear fault-bend folding. *AAPG Memoir*, *82*, 303–323.

Teng, L. S. (1990). Geotectonic evolution of late Cenozoic arc-continent collision in Taiwan. *Tectonophysics*, *183*(1-4), 57–76. https://doi.org/10.1016/0040-1951(90)90188-E

Thomas, M. Y., Avouac, J.-P., Gratier, J.-P., & Lee, J.-C. (2014). Lithological control on the deformation mechanism and the mode of fault slip on the Longitudinal Valley Fault, Taiwan. *Tectonophysics*, *632*, 48–63. https://doi.org/10.1016/j.tecto.2014.05.038

Tsai, M.-C., Yu, S.-B., Shin, T.-C., Kuo, K.-W., Leu, P.-L., Chang, C.-H., & Ho, M.-Y. (2015). Velocity field derived from Taiwan continuous GPS array (2007–2013). *Terrestrial, Atmospheric and Oceanic Sciences*, *26*(5), 527–556. https://doi.org/10.3319/TAO.2015.05.21.01(T)

Tung, H., (2008). Analysis of surface deformation based on PS-InSAR technique: Case studies in Coastal Plain, SW Taiwan (Masters Thesis). National Taiwan University, Taipei.

Wang, S.-J., Lee, C.-H., Chen, J.-W., & Hsu, K.-C. (2015). Combining gray system and poroelastic models to investigate subsidence problems in Tainan, Taiwan. *Environmental Earth Sciences*, *73*(11), 7237–7253. https://doi.org/10.1007/s12665-014-3902-5

Wang, W., Yin, H., Jia, D., Wu, Z., Wu, C., & Zhou, P. (2018). Calculating detachment depth and dip angle in sedimentary wedges using the area–depth graph. *Journal of Structural Geology*, *107*, 1–11. https://doi.org/10.1016/j.jsg.2017.11.014

Wang, Y.-J., Chan, C.-H., Lee, Y.-T., Ma, K.-F., Shyu, J. B. H., Rau, R.-J., & Cheng, C.-T. (2016). Probabilistic seismic hazard assessment for Taiwan. *Terrestrial, Atmospheric and Oceanic Sciences*, *27*(3), 325–340. https://doi.org/10.3319/TAO.2016.05.03.01(TEM)

Wu, I.-C., Chen, Y.-L., Wu, C.-I., Hsiuan, T.-H., Wu, J.-C., & Chen, H.-T., (1993). Estimation of pore pressure gradient in the Lungchuan area (Ann. Explor. Prod. No. 16). Chinese Petroleum Corporation.

Wu, Y.-Y., Hu, J.-C., Lin, G.-P., Chang, C.-P., Tung, H., & Lu, C.-H. (2013). Transient active deformation in Tainan tableland using persistent scatterers SAR interferometry. *Bulletin de la Société Géologique de France*, *184*(4-5), 441–450. https://doi.org/10.2113/gssgfbull.184.4-5.441

Yang, K.-M., Huang, S.-T., Wu, J.-C., Ting, H.-H., & Mei, W.-W. (2006). Review and new insights on foreland tectonics in western Taiwan. *International Geology Review*, *48*(10), 910–941. https://doi.org/10.2747/0020-6814.48.10.910

Yang, K.-M., Rau, R.-J., Chang, H.-Y., Hsieh, C.-Y., Ting, H.-H., Huang, S.-T., et al. (2016). The role of basement-involved normal faults in the recent tectonics of western Taiwan. *Geological Magazine*, *153*(5-6), 1166–1191. https://doi.org/10.1017/S0016756816000637

Yu, S.-B., Chen, H.-Y., & Kuo, L.-C. (1997). Velocity field of GPS stations in the Taiwan area. *Tectonophysics*, *274*(1-3), 41–59. https://doi.org/10.1016/S0040-1951(96)00297-1

Yuan, J., Huang, S.-T., Chou, T.-F., Wu, J.-C., & Lu, D.-L. (1987). The origin of the abnormal pressure zones in Southwestern Taiwan. *Annals of Exploration and Production (CPC).*, *10*, 1–27.

Yue, L.-F., & Suppe, J. (2014). Regional pore-fluid pressures in the active western Taiwan thrust belt: A test of the classic Hubbert-Rubey fault-weakening hypothesis. *Journal of Structural Geology*, *69*, 493–518. https://doi.org/10.1016/j.jsg.2014.08.002

Yue, L.-F., Suppe, J., & Hung, J.-H. (2011). Two contrasting kinematic styles of active folding above thrust ramps, western Taiwan. *AAPG Memoir*, *94*, 153–186. https://doi.org/10.1306/13251337M943431

References From the Supporting Information

Stuiver, M., Reimer, P. J., Reimer, R. W., (2018). Radiocarbon calibration CALIB 7.1, WWW program.